Environmental sensitivities of shallow-cumulus dilution – Part 2: Vertical wind profile

Sonja Drueke[1], Daniel J. Kirshbaum[1], and Pavlos Kollias[2]

[1]Department of Atmospheric and Oceanic Sciences, McGill University, Montréal, QC, Canada
[2]School of Marine and Atmospheric Sciences, Stony Brook University, Stony Brook, NY, USA

Correspondence: Sonja Drueke (sonja.drueke@mail.mcgill.ca)

Abstract. This second part of a numerical study on shallow-cumulus dilution focuses on the sensitivity of cloud dilution to changes in the vertical wind profile. Insights are obtained through large-eddy simulations of maritime and continental cloud fields. In these simulations, the speed of the initially uniform geostrophic wind, and the strength of geostrophic vertical wind shear in the cloud and subcloud layer are varied. Increases in the cloud-layer vertical wind shear (up to 9 m s^{-1} km^{-1}) lead to 40–50 % larger cloud-core dilution rates compared to their respective unsheared counterparts. When the background wind speed, on the other hand, is enhanced by up to 10 m s^{-1} and subcloud-layer vertical wind shear develops or is initially prescribed, the dilution rate decreases by up to 25 %. The sensitivities of the dilution rate are linked to the updraft strength and the properties of the entrained air. Increases in the wind speed or vertical wind shear result in lower vertical velocities across all sets of experiments with stronger reductions in the cloud-layer wind shear simulation (27–47 %). Weaker updrafts are exposed to mixing with the drier surrounding air for a longer time period, allowing more entrainment to occur (i.e., the "core exposure effect"). However, reduced vertical velocities, in concert with increased cloud-layer turbulence, also assist in widening the humid shell surrounding the cloud cores, leading to entrainment of more humid air (i.e., the "core-shell dilution effect"). In the experiments with cloud-layer vertical wind shear, the core exposure effect dominates and the cloud-core dilution increases with increasing shear. Conversely, when the wind speed is increased and subcloud-layer vertical wind shear develops or is imposed, the core-shell dilution effect dominates to induce a buffering effect. The sensitivities are generally stronger in the maritime simulations, where weaker sensible heat fluxes lead to narrower, more tilted, and, therefore, more suppressed cumuli when cloud-layer shear is imposed. Moreover, in the experiments with subcloud wind shear, the weaker baseline turbulence in the maritime case allows for a larger turbulence enhancement, resulting in a widening of the transition zones between the cores and their environment, leading to the entrainment of more humid air.

1 Introduction

Shallow cumuli are strongly affected by the ingestion of surrounding air, a process known as entrainment. Entrainment is caused by turbulent circulations that generate mixing along the cloud boundaries ("turbulent" entrainment) as well as cloud-scale dynamical circulations that draw organized inflow ("dynamic" entrainment) (e.g., Houghton and Cramer, 1951; de Rooy et al., 2013). Entrainment leads to the dilution of cloudy updrafts through mixing with drier and cooler air, which evaporates

25 cloud hydrometeors and reduces the updraft buoyancy. As a result, it tends to suppress vertical cloud development (e.g., Derbyshire et al., 2004; Gerber et al., 2008; Krueger, 2008; Del Genio, 2012; Lu et al., 2013).

Traditionally, entrainment has been conceptualized as a direct exchange of air between clouds and their undisturbed environment (e.g., Betts, 1975; Siebesma and Cuijpers, 1995; Siebesma, 1998; de Rooy et al., 2013). More recently, however, attention has turned to the importance of the thin "shell" of air surrounding the cloud in buffering the mixing process (e.g.,
30 Heus and Jonker, 2008; Wang and Geerts, 2010; Dawe and Austin, 2011; Lamer et al., 2015; Hannah, 2017; Endo et al., 2019; McMichael et al., 2020). The shell contains a mixture of cloud and environmental air, and thus represents a transition zone between in-cloud and environmental conditions. Importantly, air entrained from the shell causes less dilution than air entrained from the undisturbed environment.

The term "shell" has been used to describe different parts of a cumulus cloud. Heus and Jonker (2008) define the "cloud shell"
35 as the subsiding air at the cloud edge and outside the cloud, which tends to be more humid than the surrounding environment. In cloud simulations, Hannah (2017) referred to the "cloudy shell" as the cloudy grid points surrounding the cloud core, where the core is the positively buoyant and ascending portion of the cloud. Also, Dawe and Austin (2011) defined the "cloud-core shell" as the grid points immediately adjacent to the cloud core (whether cloudy or not). Although each definition is slightly different, they all refer to buffer zones immediately surrounding a cloud or cloud core.

40 The dilution experienced by shallow cumuli is partially controlled by environmental conditions. In the first part of this study, we used LES to investigate the impacts of selected thermodynamics conditions on the cloud-core dilution (Drueke et al., 2020). The core dilution rate was found to correlate strongly, and positively, with cloud-layer relative humidity (RH), consistent with various studies (e.g., Wang and McFarquhar, 2008; Stirling and Stratton, 2012; Lu et al., 2018; Bera and Prabha, 2019). This finding can be explained by a simple buoyancy-sorting argument. Drueke et al. (2020) also found a strong sensitivity of shallow-
45 cumulus dilution to continentality, in that simulated maritime cumuli experienced about twice the dilution of corresponding continental cumuli. The sensitivity was linked to larger cloud-base mass fluxes over land, driven by stronger sensible heat fluxes and subcloud turbulence. Additionally, Drueke et al. (2020) found the cloud dilution to be relatively insensitive to cloud- and subcloud-layer depths. A doubling of the former resulted in only a 2–3 % change of the dilution rate and a 50 % increase in the latter resulted in only a 4 % decrease in dilution.

50 A consistent theme in LES cloud studies is that wider clouds tend to undergo less dilution, become more vigorous, and undergo deeper ascent than narrower clouds (Khairoutdinov and Randall, 2006; Kirshbaum and Grant, 2012; Rieck et al., 2014; Rousseau-Rizzi et al., 2017). The concept of cloud radius (R) regulating cloud dilution has prevailed for decades (e.g., Morton, 1957), and can be explained by the notion that, as R increases, the entrainment flux into the cloud, which depends on the cloud circumference, cannot keep pace with the increasing cloud cross-sectional area. While Drueke et al. (2020) also
55 found a generally strong correlation between cloud width and cloud dilution, it was not universal. Thus, while R is an important controlling parameter, its effects may be overwhelmed by other factors.

Cloud vertical velocity (w) is also strongly related to cloud dilution. Although a robust inverse relationship between the bulk dilution rate (ε) and w has been reported in LES (Neggers et al., 2002; Tian and Kuang, 2016; Lu et al., 2018) and observations (Kirshbaum and Lamer, 2021), the mechanisms behind this trend are unclear. From one perspective, dilution may

be thought to control w by reducing cloud buoyancy and mixing lower-w surrounding air into the cloud. While recent LES studies suggest that the latter "direct" effect is weak (e.g., de Roode et al., 2012; Sherwood et al., 2013; Romps and Charn, 2015), the corresponding entrainment-induced buoyancy loss remains important. From the opposite perspective, cloud dilution may be thought to depend on w, because w determines the time scale over which clouds are exposed to environmental air (Neggers et al., 2002).

The present study focuses on the sensitivity of shallow-cumulus dilution to the geostrophic vertical wind profile. While vertical wind shear is known to organize deep convection into particularly intense manifestations (e.g., supercell thunderstorms), it has more subtle effects on shallow cumuli. In principle, this shear can enhance cloud entrainment via increased turbulent mixing and/or stronger cloud-relative winds (e.g., Markowski and Richardson, 2010). Moreover, the shear tilts moist thermals downshear with height (e.g., Malkus, 1952; Asai, 1964), which enhances adverse vertical perturbation pressure gradients to weaken updraft accelerations (e.g., Parker, 2010; Peters, 2016; Helfer et al., 2020). Linear theory suggests that this shear-induced updraft suppression depends on cloud width, with the strongest suppression for the narrowest, most vertically tilted, clouds (Kirshbaum and Straub, 2019).

Vertical wind shear also tends to displace the cloud core from the cloud center, with the maximum buoyancy, vertical velocity and liquid water content all shifting to the upshear side of the cloud (e.g., Heus and Jonker, 2008). This asymmetry is consistent with the linear theory of Rotunno and Klemp (1982), who showed that vertical shear induces a perturbation pressure dipole across the updraft with high pressure on the upshear flank and low pressure on the downshear flank. These pressure anomalies cause the impinging flow to divert around the upshear side of the cloud and converge on the downshear side. As a result, the upshear side exhibits weakened dilution while the downshear side exhibits enhanced dilution (e.g., Heymsfield et al., 1978; Zhao and Austin, 2005). Similar to flow separation around a mountain barrier (e.g., Smolarkiewicz and Rotunno, 1989), a turbulent and moist wake also forms downshear of the cloud (e.g., Perry and Hobbs, 1996; Heus and Jonker, 2008).

Despite receiving significant attention, the impacts of vertical wind shear on ε remain unclear. Both numerical simulations (Brown, 1999; Lin, 1999; Helfer et al., 2020) and observational ε retrievals (Kirshbaum and Lamer, 2021) suggest minimal sensitivity of ε to cloud-layer shear. However, these findings counter the logic of Neggers et al. (2002) that weaker updrafts (here, due to shear-enhanced vertical perturbation pressure gradients) should enhance cloud dilution. To resolve this apparent contradiction, more detailed analyses of the impacts of vertical wind shear on shallow cumuli are needed. Furthermore, little attention has been paid to the general impact of background winds on shallow-cumulus dilution. Although a uniform background flow does not directly impact cumuli, it may indirectly affect them by modifying the subcloud flow. As the background winds increase, so does the frictionally induced vertical shear in the subcloud layer, which can extend into the cloud layer and/or organize the subcloud turbulence into shear-parallel rolls (e.g., Weckwerth et al., 1997). The latter are associated with elongated updrafts in the shear direction that, upon reaching saturation at cloud base, may give rise to larger and less dilute cumuli. For the special case of supercells, Peters et al. (2019b) found that stronger vertical wind shear may indirectly weaken cloud dilution by enhancing cloud inflow and cell width.

While no studies to our knowledge have directly investigated the relationship between background winds and cloud dilution, some offer insights into how simulated clouds may respond to increased wind speeds. Nuijens and Stevens (2012) found a

positive correlation between background wind speed and cloud depth in simulated trade-wind cumuli, an effect that may have been accompanied by decreased cloud dilution. Also, from a purely numerical perspective, the degree of model diffusion is sensitive to cross-grid wind speed. Cloud models typically use highly diffusive flux-limited, flux-corrected, and/or monotonic advection schemes to damp spurious small-scale oscillations generated by advective errors near cloud surfaces. In the presence of a cross-grid flow, these schemes tend to produce enhanced diffusion in the flow direction, which can spuriously enhance cloud size and thereby weaken cloud dilution (Wyant et al., 2018).

To study the impacts of the vertical wind profile on shallow-cumulus dilution, we conduct LES of shallow-cumulus ensembles in which aspects of this wind profile are systematically varied. The model configuration is provided in Sect. 2, and the experimental results are presented in Sect. 3. Sect. 4 provides a physical explanation of the various sensitivities of cloud dilution, and proposes a new empirical formulation for the dilution rate. Section 5 provides the conclusions.

2   Methodology

2.1   Model configuration

As in Part I of this study, we conduct LES of shallow cumulus ensembles using the Bryan Cloud Model version 17 (CM1; Bryan and Fritsch, 2002). In LES mode, CM1 accurately reproduces the findings from past LES inter-comparison studies of shallow cumuli (Drueke et al., 2019, 2020). To examine diverse cloud fields, we consider one maritime case and one continental case, the former based on the LES inter-comparison study of the Barbados Oceanographic and Meteorological Experiment (BOMEX) by Siebesma et al. (2003), and the latter based on the LES inter-comparison of shallow cumuli at the US Atmospheric Radiation Measurement (ARM) Southern Great Plains (SGP) observatory in Oklahoma (Brown et al., 2002).

The model configuration is similar to that in Drueke et al. (2020), with a monotonic fifth-order weighted essentially non-oscillatory (WENO) advection scheme for both scalars and velocity, a third-order Runge-Kutta time-differencing scheme, and periodic horizontal, semi-slip lower, and free-slip upper boundary conditions as well as a f-plane approximation. The Coriolis force is applied to wind perturbations from the initial, geostrophic profile. A horizontal grid spacing of 32 m is used to adequately resolve the turbulent circulations of interest. The BOMEX horizontal domain size of 6.4×6.4 km^2 is left unchanged from Siebesma et al. (2003), while the ARM-SGP domain size is doubled from 6.4×6.4 km^2 in Brown et al. (2002) to 12.8×12.8 km^2 to capture the larger-scale circulations of this cloud field. For each experiment, an ensemble of six members is conducted, each with a different field of small-amplitude random perturbations added to the initial potential temperature and water-vapor mixing ratio fields. The results presented for each case are averaged over this ensemble.

2.2   LES experiments

We conduct various idealized experiments to quantify the impacts of the initial wind profile on the cloud dilution. To examine the impacts of cloud-layer vertical shear, the first set of experiments (CL-SHR) initializes zero wind in the subcloud layer and positive, linear westerly vertical shear in the cloud layer (Fig. 1). While the absence of subcloud winds differs from the

standard configurations of these cases, it limits the development of subcloud vertical shear that, as will be seen, may indirectly affect cloud dilution. To ensure that the shear layer is fully contained within the cloud layer, the shear base is placed at 720 m in BOMEX and 1000 m in ARM-SGP (dashed lines in Fig. 1). Zonal vertical shears ranging from 0 to 9 m s^{-1} km^{-1} (CTRL to S9), in increments of 3 m s^{-1} km^{-1}, are applied from the shear base to the domain top. For BOMEX, we also include an experiment with vertical wind shear of 1.8 m s^{-1} km^{-1}, matching that of Siebesma et al. (2003) (Table 1).
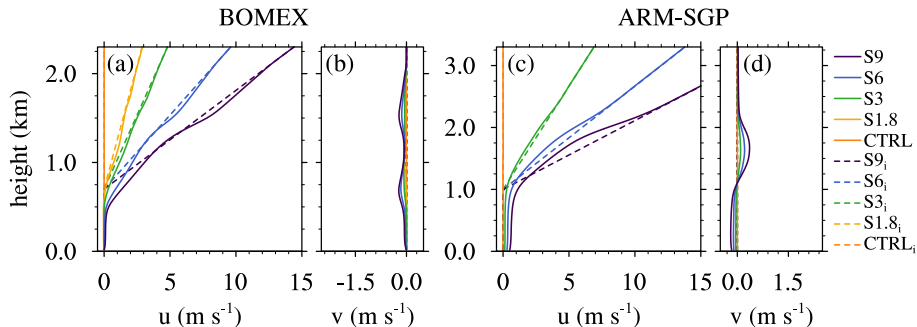
Figure 1. Initial wind profiles (dashed lines) and wind profiles averaged over the analysis period (solid lines) for the CL-SHR (**a-b**) BOMEX (3-6 h) and (**c-d**) ARM-SGP (14:00-15:00 LST) experiments.

Table 1. Summary of CL-SHR experiments. See text for further details.

	BOMEX	ARM-SGP
CTRL	x	x
S1.8	x	-
S3	x	x
S6	x	x
S9	x	x

In a second set of experiments (WIND), we evaluate the sensitivity of simulated cloud dilution to vertically uniform zonal geostrophic winds of magnitude U. In line with the prevailing wind directions at the two locations, we consider easterly winds in BOMEX and westerly winds in ARM-SGP (Table 2). The winds increase from zero (CTRL) up to 10 m s^{-1} (U10; dashed lines in Figs. 2a-d). Finally, to examine the impacts of subcloud geostrophic vertical shear on cloud dilution, a third suite of experiments vary the near-surface shear (SCL-SHR). These profiles are identical to those in WIND except for having zero surface wind and a layer of linear zonal shear over the lowest 250 m (dashed lines in Fig. 2e and g). Individual simulations from this suite of experiments are named based on their shear magnitude; for example, the case of 40 m s^{-1} km^{-1} of near-surface shear is named US40.

Due to the short durations of active cloud development (< 6 h) in the BOMEX and ARM-SGP simulations, we do not apply any forcings to maintain the wind profile at its initial values. The wind profiles thus vary with time, mainly through the action of subcloud and cloud-layer vertical mixing. Nevertheless, as will be seen, the qualitative differences between the

Table 2. Summary of the WIND and SCL-SHR experiments. See text for further details.

	BOMEX	ARM-SGP
WIND (m s^{-1})		
CTRL	0.0	0.0
U2.5	-2.5	2.5
U5	-5.0	5.0
U10	-10.0	10.0
SCL-SHR (m s^{-1} km^{-1})		
CTRL	0.0	0.0
US10	-10.0	10.0
US20	-20.0	20.0
US40	-40.0	40.0
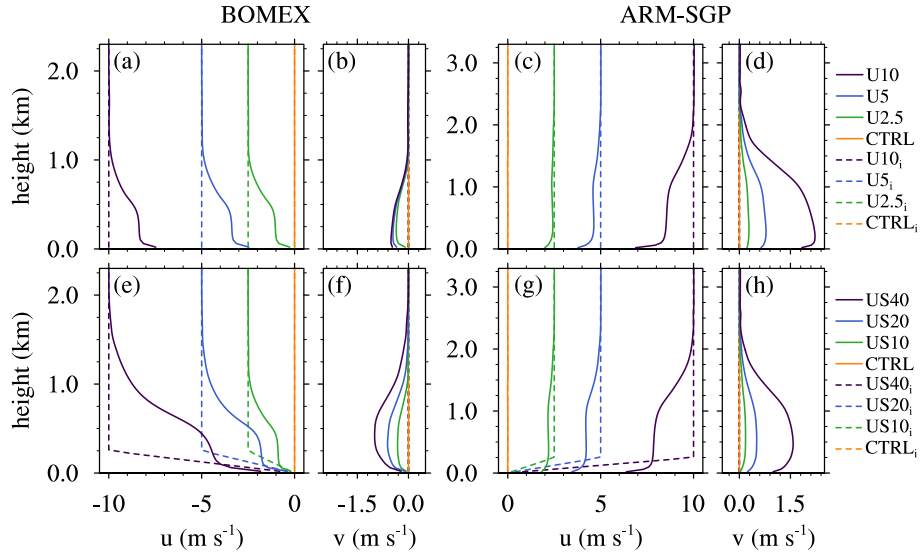
Figure 2. Initial wind profiles (dashes lines) and wind profiles averaged over the analysis period (solid lines) for (**a-b**) the BOMEX and (**c-b**) the ARM-SGP WIND experiments and (**e-f**) the BOMEX and (**g-h**) the ARM-SGP SCL-SHR experiments.

various cases are maintained throughout the simulations, although slightly reduced over time (see solid lines in Figs. 1-2). To determine whether sensitivities to cross-grid flow like those highlighted by Wyant et al. (2018) affect our model results, we have compared various runs with a fixed and a translating grid (at the approximate average speed of the cloud-layer flow).
145 The differences between these runs were minimal, suggesting that such effects are not significant for our model configuration. Therefore, for consistency, all simulations described herein use a stationary grid.

3 Results overview

3.1 The CTRL cases

The maritime BOMEX CTRL case represents a typical trade-wind cloud field, except for the lack of ambient winds. The
150 surface heat fluxes, large-scale advection and subsidence tendencies, and simulated convection come into balance to yield a statistically quasi-steady flow over 3-6 h (Siebesma et al., 2003). The cloud base stays at roughly 500 m throughout the simulation, and the cloud top extends above the base of the trade-wind inversion at 1.5 km (Fig. 1 of Drueke et al., 2020). A horizontal cross-section of w at the midpoint of the subcloud layer and a time of 4 h shows a cellular turbulence pattern with variations on a broadly similar scale (~ 500 m) as the subcloud layer depth (Fig. 3a). The small-scale subcloud turbulence
155 gives rise to small active cumuli with mean radii at the level of free convection (R_{LFC}) of 80 m (Fig. 3c). Active clouds are defined as clouds possessing a positively buoyant and ascending internal core, and a circular cloud shape is used to infer R_{LFC} based on the horizontal area occupied by the cloud.

The continental ARM-SGP CTRL case, in contrast, exhibits a time-evolving cloud field forced by the diurnal cycle of the surface heat fluxes (Brown et al., 2002). Shallow cumuli first initiate at about 11:00 local solar time (LST) and dissipate by
160 around 20:00 LST. Over that time, the cloud base rises from 0.6 km to 1.3 km (Drueke et al., 2020). As shown by the w cross-section at the midpoint of the subcloud layer at 13:15 LST (Fig. 3b), the deeper subcloud layer in ARM-SGP gives rise to larger horizontal circulations than in BOMEX. As a result, R_{LFC} in ARM-SGP is larger (Fig. 3d), with an averaged value (207 m) more than double that of BOMEX. The cloud droplet number concentration is smaller in the maritime BOMEX experiments (100 cm^{-3}) than in the continental ARM-SGP simulations (250 cm^{-3}).
165 Based on the time-evolution of the BOMEX and ARM-SGP simulations, we define analysis periods to be used for the detailed calculations to follow. These periods are selected to avoid model spin-up or cloudless intervals, thus focusing on the well developed turbulent cloud fields of interest. The quasi-stationarity of the BOMEX case permits the use of a relatively long 3-h averaging period, covering 3-6 h. Due to the diurnal evolution of the cloud field in the continental ARM-SGP experiments, a shorter averaging time of one hour is used, running from 14:00-15:00 LST. Unless otherwise specified, all calculations herein
170 are conducted during these analysis periods.
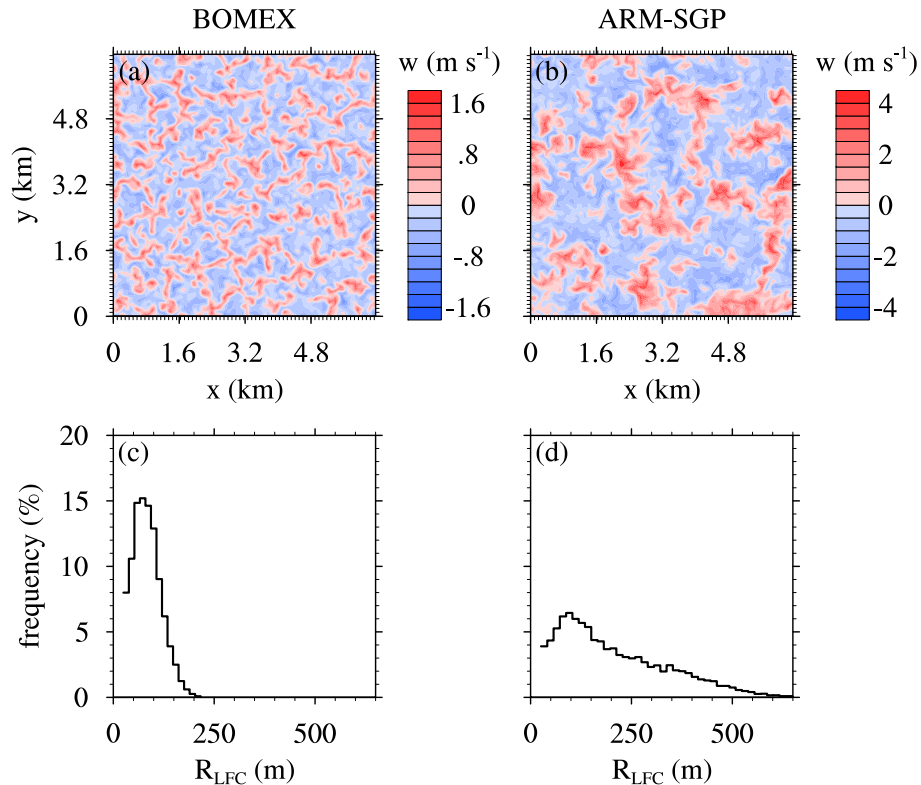
Figure 3. Instantaneous cross-section of the vertical velocity at the midpoint of the subcloud layer of the CTRL experiments in (**a**) BOMEX at 4 h and (**b**) ARM-SGP at 13:15 LST. For ARM-SGP, a subsection of equal size to the BOMEX domain is shown. (**c-d**) The histogram of the cloud radius at LFC of all active clouds. Panels (**a**) and (**c**) show the maritime BOMEX case, and the panels (**b**) and (**d**) the continental ARM-SGP case.

3.2 Sensitivity to cloud-layer vertical wind shear

Over the course of the BOMEX CL-SHR simulations, the shear base lowers from its initial value (720 m) down to about 500 m due to cloud-layer vertical mixing. As a result, the cloud base and shear base nearly coincide over the analysis period (solid lines in Figs. 1a-b). The flow remains predominately westerly with a weak northerly component in the cloud layer.

175 Similarly, in the ARM-SGP CL-SHR simulations, the shear base over the analysis period roughly coincides with the cloud base at 1050 m (Figs. 1c-d). Although the subcloud winds remain weak, they turn more northerly due to larger surface drag, enhanced turbulent mixing, and a stronger Coriolis force. In both cases, the cloud-layer shear weakens modestly over time (Figs. 1a and c). In the most extreme S9 case, the cloud-mass-flux-weighted shear weakens to 6.4 m s^{-1} km^{-1} (BOMEX) and 6.9 m s^{-1} km^{-1} (ARM-SGP) over the analysis period, a reduction of around 25 %. Thus, despite the gradually weakening

180 shear, the two sets of simulations exhibit comparable shear magnitudes throughout.

As the cloud-layer shear is increased, the subcloud layer is minimally affected, with similar w fields in the CTRL and S9 cases (cf. Figs. 3a-d and Figs. 4a-b). In the cloud layer, the clouds widen with increasing shear, a signal that extends down to the LFC. The R_{LFC} distributions shift toward larger scales in both BOMEX and ARM-SGP (Figs. 4c-d), but much more so in BOMEX. The mean R_{LFC} increases by 27 % in BOMEX, compared to 14 % in ARM-SGP.
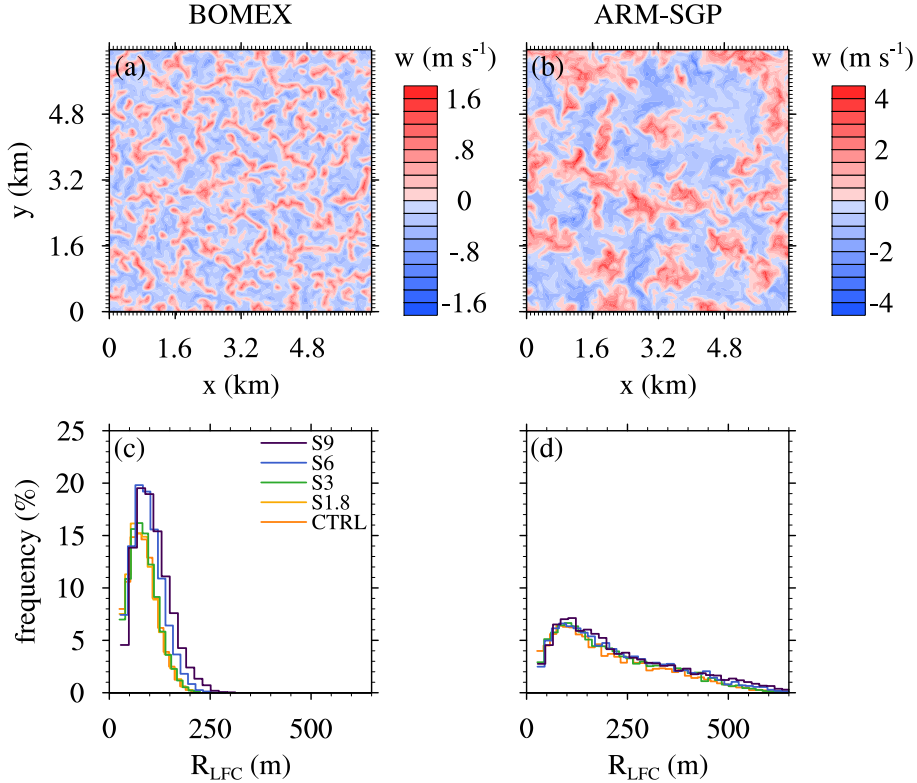
Figure 4. As in Fig. 3 but for the CL-SHR experiments with panel (**a**) and (**b**) showing the horizontal cross-section of the vertical velocity at the subcloud-layer midpoint of the S9 experiments.

185 Although not shown for brevity, the simulated cumuli respond to the imposed vertical shear in expected ways: (i) they tilt downshear with height (e.g., Malkus, 1952; Asai, 1964), (ii) they develop pressure-anomaly dipoles straddling the clouds along the shear axis, with high pressure upshear and low pressure downshear (e.g., Rotunno and Klemp, 1982; Zhao and Austin, 2005), and (iii) their buoyant cloud cores shift to the upshear side of the cloud (e.g., Heymsfield et al., 1978; Heus and Jonker, 2008). Moreover, the cloud-top heights decrease under stronger vertical shear, suggesting a shear-induced cloud

190 suppression. Compared to the CTRL experiments, the cloud-top height decreases by 15–20 % in the S9 versions of the BOMEX and ARM-SGP cases (not shown).

  Diagnosis of the simulated bulk fractional entrainment rate, or simply the "dilution rate", follows the formulation of Siebesma and Cuijpers (1995, hereafter SC95). This quantity measures how much pure environmental would need to be entrained to achieve the simulated core dilution. Contrary to direct entrainment calculations, it does not quantify the actual

195 mixing across the cloud perimeter. Dilution is evaluated based on the budget of the total water specific humidity (s_t)

$$E\left(s_{t_{env}} - s_{t_{co}}\right) = M_{co}\frac{\partial s_{t_{co}}}{\partial z} + \frac{\partial a_{co}\rho\overline{w's_t'}^{co}}{\partial z} + a_{co}\rho\frac{\partial s_{t_{co}}}{\partial t} - a_{co}\rho\left(\frac{\partial \overline{s_t}}{\partial t}\right)_{forcing} , \tag{1}$$

where E represents the bulk entrainment rate. The subscript "co" denotes conditional averages within cloud cores and "env" indicated the averages over the environment, defined as all non-core regions. The core mass flux (M_{co}) is defined as $M_{co} = \rho a_{co}w_{co}$, where ρ is the air density, a_{co} the cloud-core fraction, and w the vertical velocity. The plain overbar denotes the

200 horizontal domain average, while the overbar indexed 'co' represents the conditional average of the fluctuations of the cloud cores with respect to the cloud-core average. The right-hand side of Eq. (1) considers the changes to the conserved s_t with height (z) and in time (t), along with changes to s_t owing to vertical turbulent fluxes and large-scale forcings. To obtain the bulk dilution rate (ε), we divide E by M_{co}. Instantaneous vertical profiles of ε are calculated at each model output time over the full horizontal domain, at all vertical levels where cloud core grid points are found. To compare ε across the different

205 simulations, we perform some averaging to obtain representative values. First, 15-min running averages are calculated from the 5-min model output data, from which bulk cloud-layer averages are computed over the central 50 % of the cloud layer. Both the vertical profiles and the bulk values are then averaged over the analysis period.

The ε profiles thus obtained increase monotonically with vertical wind shear (Fig. 5). This sensitivity originates at cloud base, increases to a maximum near the cloud-layer midpoint, and decreases rapidly near cloud top. Averaged over the central

210 50 % of the cloud layer, ε in the BOMEX S9 experiment (2.6 km^{-1}) is about 50 % larger than in the CTRL simulation (1.7 km^{-1}). This sensitivity is comparable but slightly weaker ($\sim$ 40 %) in ARM-SGP.
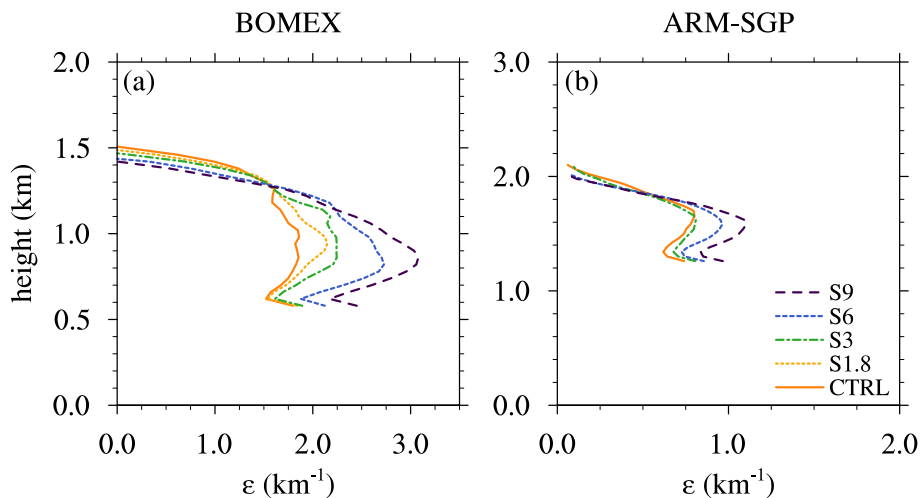
Figure 5. Dilution rate (ε) for the CL-SHR experiments for **(a)** BOMEX and **(b)** ARM-SGP.

3.3 Sensitivity to vertically uniform geostrophic winds

The initially uniform zonal velocity profiles from the WIND simulations evolve into vertically varying profiles with strong low-level vertical shear. At analysis time, the zonal wind is strongly forward-sheared near the surface, exhibits a nearly constant value within the central part of the subcloud layer, and then exhibits additional forward shear extending into the lower cloud layer (Figs. 2a, c). The Coriolis force induces a cyclonic turning of these frictionally decelerated winds, leading to a meridional wind component that is maximized within the subcloud layer (Figs. 2b, d). As with the CL-SHR experiments, the stronger surface drag and Coriolis force in ARM-SGP leads to stronger frictional deceleration and cyclonic wind turning than in the corresponding BOMEX simulations.

In BOMEX U10, the low-level shear organizes the subcloud flow into longitudinal bands, or rolls, aligned with the low-level winds (Fig. 6a), which contrasts with the more disorganized convection in ARM-SGP U10 (Fig. 6b). These differing responses likely stem from the different surface heating rates in the two cases. The larger surface buoyancy flux in ARM-SGP yields a more buoyancy-dominated convective boundary layer (CBL), which overwhelms any shear-induced turbulence organization. The potential for convective rolls may be assessed based on the Monin-Obukhov length (L), where L represents the height at which buoyancy dominates over shear in the production of TKE:

$$
L = -\frac{\overline{\theta}_v \left(\left(\overline{u'w'} \right)^2 + \left(\overline{u'w'} \right)^2 \right)^{0.75}}{kg\overline{w'\theta'_v}} ,
\tag{2}
$$

$k = 0.4$ is the von-Kármán constant, g is the gravitational acceleration, θ_v is the virtual potential temperature, u, v, and w are x, y, and z wind components, primes denote perturbations from a temporal or spatial average (denoted by overbars), and all quantities are evaluated at the surface (e.g., Stull, 1985). Negative L corresponds to CBLs, with smaller magnitudes reflecting more dominant buoyancy production.

Taking z_i as the subcloud-layer depth and evaluating L at the surface, and summing resolved and subgrid fluxes in Eq. (2), we obtain $-z_i/L = 1.6$ and $-z_i/L = 9.5$ for the BOMEX and ARM-SGP U10 cases, respectively. The smaller BOMEX value is more favorable for rolls, falling into the $0 \leq -z_i/L \leq 4.5$ range reported by Deardorff (1972) as conducive for roll development. This roll organization at larger U in BOMEX is associated with increased subcloud length scales: the wavelength of the spectral peak in the subcloud kinetic energy spectrum increases by about 110 % from CTRL to U10 (Fig. 6c) as the mean R_{LFC} increases by ~ 70 % (Fig. 6e). This systematic increase in cloud size with subcloud shear is consistent with the conclusion by Peters et al. (2019b) about vertical shear and updraft width in supercells. For ARM-SGP, the subcloud length scales also increase, but by a much smaller amount (20 %; Fig. 6d), and R_{LFC} increases minimally (Fig. 6f).

The BOMEX ε decreases with increasing U over most of the cloud layer, except near cloud base (Fig. 7a). Averaged over the central 50 % of the cloud layer, ε decreases by 25 % from CTRL to U10. In contrast, the ARM-SGP ε changes minimally across the experiments (Fig. 7b), with the cloud-layer-averaged ε decreasing by only 7 % from CTRL to U10. In both BOMEX and ARM-SGP, the ε sensitivity depends on height, with the dominant trend lying in the mid-to-upper cloud layer and non-systematic variations in the lower cloud layer.
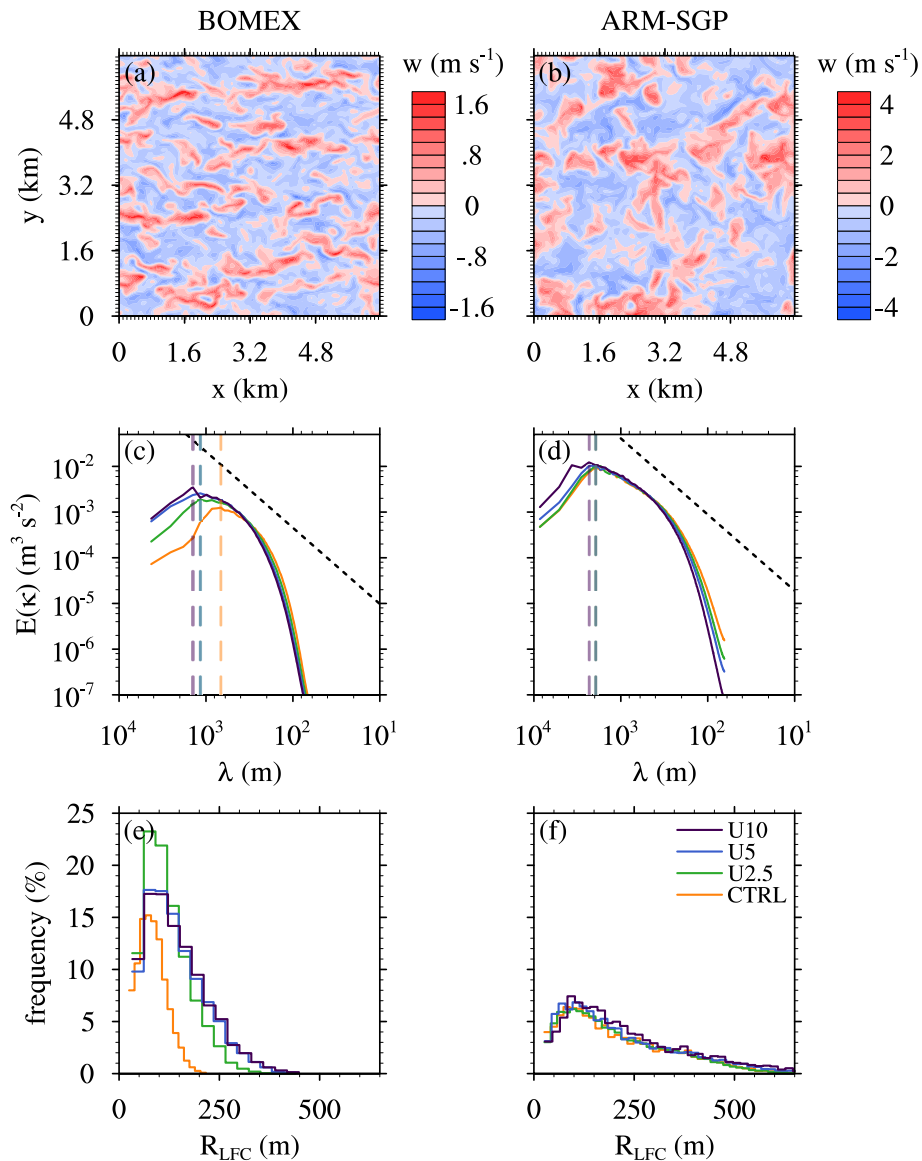
Figure 6. Similar to in Fig. 3 but for the WIND experiments with panel (**a**) and (**b**) showing horizontal cross-section of the vertical velocity halfway into the respective subcloud layer of the U10 experiments. (**c-d**) Two-dimensional kinetic-energy spectra in the subcloud layer for the same experiments. The black dashed lines shows the slope of $\kappa^{-5/3}$ and the colored dashed lines indicate the scales of maximum energy of the respective spectra. (**e-f**) The histogram of the cloud radius at LFC.

3.4 Sensitivity to subcloud-layer shear

The only initial difference between the WIND and SCL-SHR experiments is the latter's geostrophic subcloud wind shear. Although vertical mixing modifies the wind profiles over time, they maintain stronger vertical wind shear in the subcloud and lower cloud layer than the corresponding WIND cases (Figs. 2e-h). The strengthened cloud-layer shear is most pronounced in the BOMEX US40 case, where the shear extends up to 1.5 km, compared to only 1 km in the BOMEX U10 case. As in the WIND experiments, the subcloud shear tends to organize the subcloud turbulence into shear-parallel rolls in BOMEX (but not in ARM-SGP), with even larger increases in the mean of the cloud-size distribution (not shown). Again, ε generally decreases with increasing winds, with a larger cloud-layer-averaged decrease in BOMEX (22 %) than in ARM-SGP (13 %) between the CTRL and US40 cases (Figs. 7c-d).

The ε sensitivity in BOMEX is characterized by a positive trend over 0.5-0.8 km that reverses to a negative trend above (Fig. 7c). This feature may be owing to a combination of two effects, the first being the positive sensitivity of ε to vertical shear established in the CL-SHR experiments. As U increases, so does the lower-cloud-layer shear in SCL-SHR, which may yield the positive sensitivity of ε to U over the lower cloud layer (Fig. 7c). A second effect is the possibility of elevated cloud initiation by vertically propagating internal gravity waves. As previously noted, the SCL-SHR flows exhibit wider subcloud updrafts and sharper cloud-base shears as U is increased (Fig. 2e). Both factors favor vertically propagating waves via the "obstacle effect" (e.g., Gibert et al., 2011), in which wave disturbances are forced by airflow over clouds penetrating into the cloud layer. Compared to CTRL, the US40 case exhibits a much wider distribution of cloud-base heights over 0.5-0.8 km (not shown). Such heterogeneity in cloud-base height complicates the interpretation of ε, for reasons outlined in Kirshbaum (2020). Namely, vertical variations in conditionally averaged core conserved properties cannot be unambiguously attributed to cloud dilution, because they can also be explained by variations in the source layers of different clouds. Thus, the trend in ε over 0.5-0.8 km may be more reflective of variations in cloud-base height than to variations in cloud dilution.

Although the WIND and SCL-SHR experiments reach a common conclusion that subcloud-layer shear tends to decrease cloud-layer dilution, the consideration of both sets of simulations aids physical interpretation. For one thing, it shows that geostrophic shear is not required to realize this trend; even frictionally induced shear at the surface, which is present in all flows, suffices. Also, as mentioned above, the SCL-SHR experiments reveal an effect that was absent in WIND: a systematic enhancement in lower-cloud-layer dilution. Attribution of this effect to the enhanced lower-cloud-layer shear is facilitated by the WIND experiments, where the lower-cloud-layer shear and dilution vary much less between the different cases.

4 Physical interpretation

Two factors have been found to jointly explain the sensitivities of ε to the initial wind profile: the cloud-core w and the mixing fraction (μ; the fraction of core air within the cloud-core shell). In the following, we investigate each factor in detail.
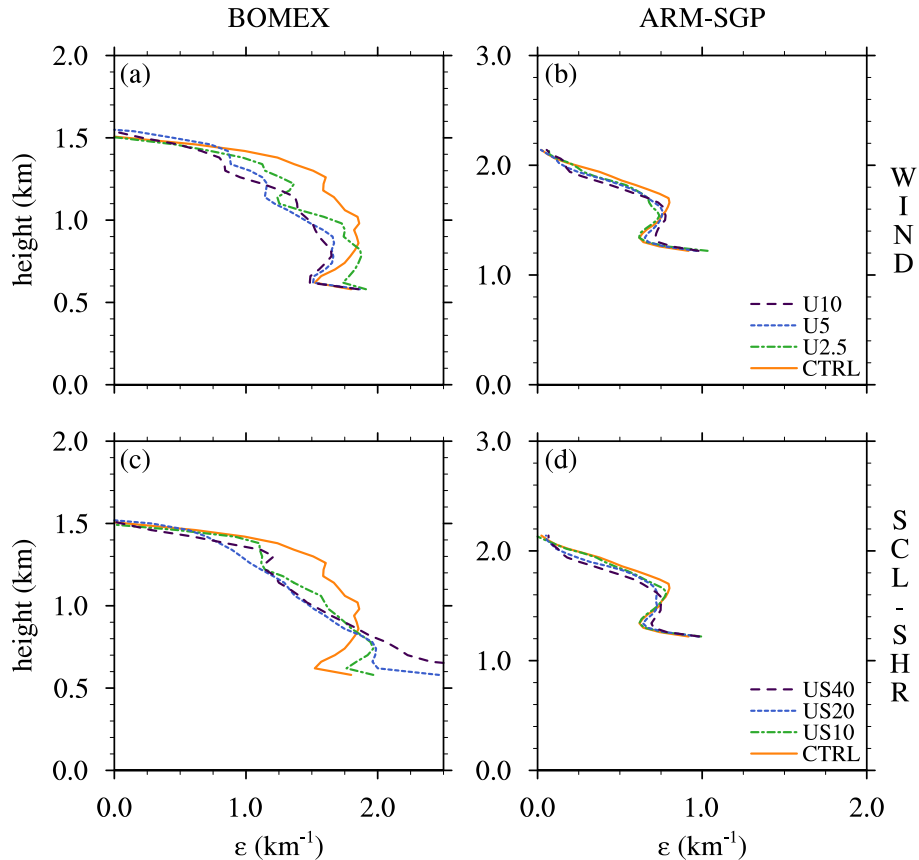
Figure 7. Dilution rate (ε) for the WIND experiments for (**a**) BOMEX and (**b**) ARM-SGP. (**c-d**) show the dilution rate profiles for the respective SCL-SHR experiments. Panels (**a**) and (**c**) are for BOMEX and panels (**b**) and (**d**) are for ARM-SGP.

4.1 Cloud-core vertical velocity

275 As mentioned in Sect. 1, the conditionally averaged cloud-core w (or w_{co}) may influence ε by controlling the time scale over which ascending clouds or cloud-cores are exposed to environmental air (e.g., Neggers et al., 2002). Although such a one-way causal sensitivity between w_{co} and ε likely oversimplifies their relationship, the correlation between w_{co} and ε still merits examination. In the CL-SHR experiments, w_{co} at cloud base is larger in ARM-SGP (2.6 m s^{-1}) than in BOMEX (1.7 m s^{-1}) (Figs. 8a-b). After a brief decrease between cloud base and the LFC, w_{co} rebounds to maxima near cloud top of 2.5-5 m s^{-1}

280 in ARM-SGP and 1-2.5 m s^{-1} in BOMEX. The larger w_{co} in ARM-SGP is owing to stronger surface heating, which drives stronger subcloud turbulence and cloud-base updrafts, in conjunction with larger cloud-core buoyancy b_{co} (Figs. 9b and d), which enhances vertical motions above the LFC.

Cloud-layer shear induces a systematic reduction in w_{co} in the CL-SHR experiments, which is expected given the tendency of this shear to tilt and weaken cumulus updrafts (e.g., Peters, 2016; Peters et al., 2019a; Helfer et al., 2020). Near cloud
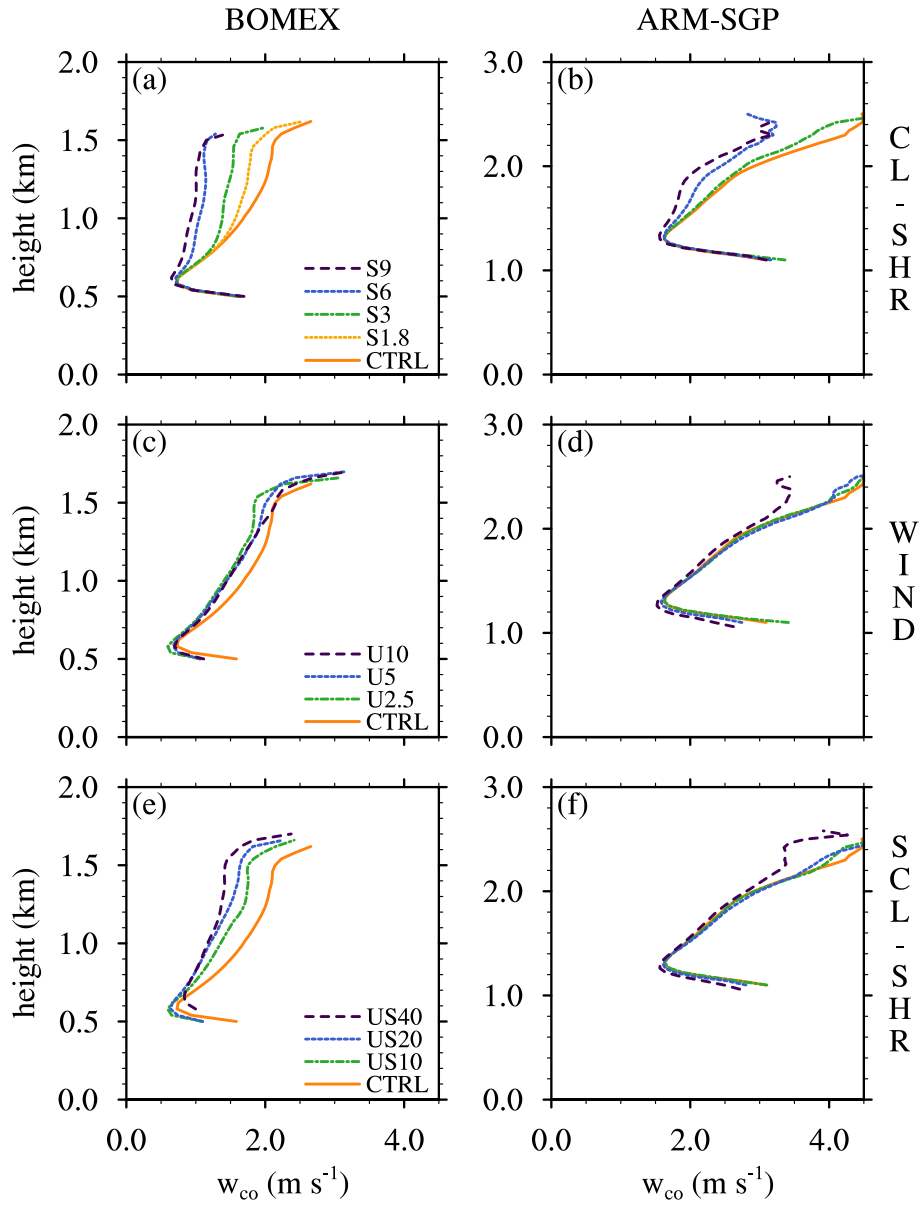
Figure 8. Vertical profiles of conditionally averaged cloud-core vertical velocities (w_{co}) for (**a-b**) the CL-SHR, (**c-d**) the WIND, and (**e-f**) the SCL-SHR experiments. Panels (**a**), (**c**), and (**e**) show the BOMEX case, and the panels (**b**), (**d**), and (**f**) the ARM-SGP one.

base, where w_{co} is dominated by subcloud momentum, the differences between the various cases are small. These differences increase with height to a maximum near the cloud tops. Averaged over the central 50 % of the cloud layer, BOMEX exhibits a 47 % decrease in w_{co} between CTRL and S9, compared to a 27 % decrease in ARM-SGP. Hence, increased cloud-layer shear is associated with decreased w_{co} and larger ε, consistent with the findings of Neggers et al. (2002).
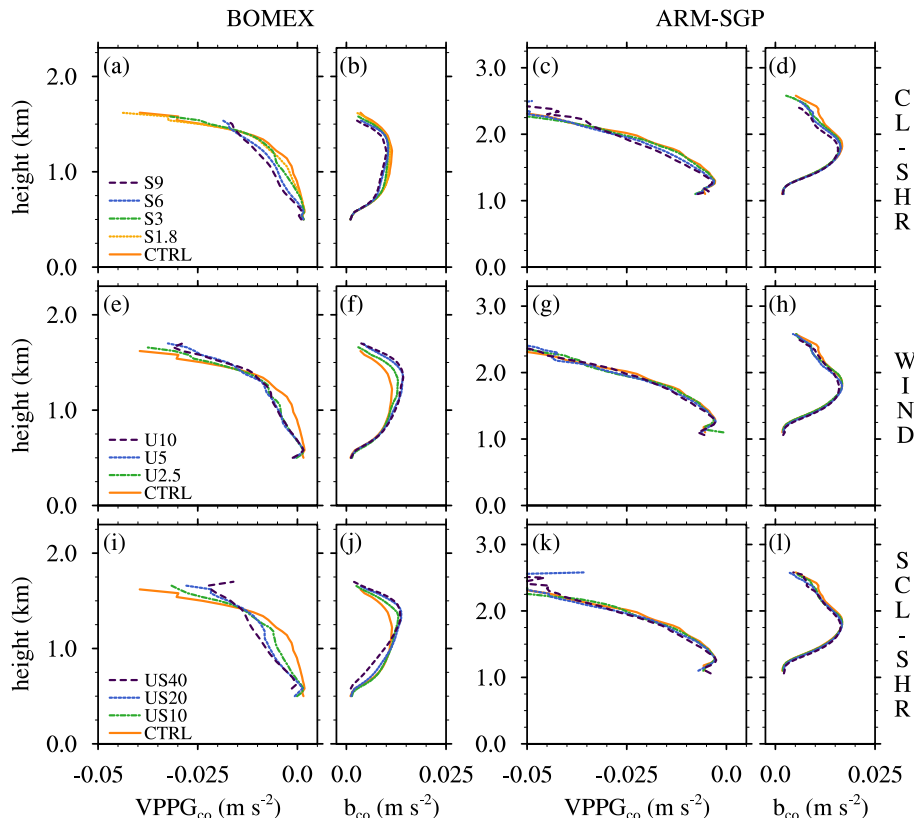
Figure 9. Vertical perturbation pressure gradients (VPPG$_{co}$) and conditionally averaged cloud-core buoyancy (b_{co}) for (**a-d**) the CL-SHR, (**e-h**) the WIND, and (**i-l**) the SCL-SHR experiments. Panels (**a-b**), (**e-f**), and (**i-j**) show the BOMEX case, and the panels (**c-d**), (**g-h**), and (**k-l**) the ARM-SGP one.

For the BOMEX WIND and SCL-SHR experiments, w_{co} is again largest in the CTRL cases and decreases with increasing U (Figs. 8c, e). Cloud-layer averages of w_{co} decrease by 8 % and 27 %, respectively, between the CTRL and the end members of each suite (U10 and US40). By contrast, the corresponding ARM-SGP experiments are nearly insensitive to U, with only a 7 % and 6 % decrease in cloud-layer-averaged w_{co}. Unlike the CL-SHR experiments where w_{co} and ε varied inversely, ε *decreases* with decreasing w_{co} in these experiments. Thus, w_{co} cannot be the only factor regulating the simulated dilution rate. Although the plot of w_{co}^{-1} against ε for all simulations indicates a large correlation coefficient ($R = 0.93$), the differing trends of the CL-SHR and WIND/SCL-SHR experiments are obvious (Fig. 10a). All continental experiments are more 'resilient' to subcloud- and cloud-layer wind shear and show weaker sensitivities to the imposed changes in geostrophic winds, particularly

in the WIND and SCL-SHR experiments. When only the maritime experiments are considered, the correlation coefficient between ε and w_{co} is substantially reduced ($R = 0.65$). Thus, while w_{co} strongly influences (and/or is influenced by) ε, other factor(s) must also be important.
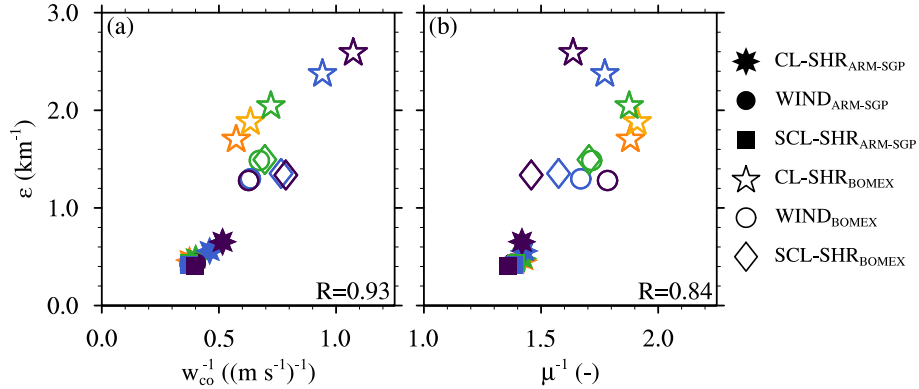
Figure 10. Variation of simulated dilution rate (ε) with (**a**) conditionally averaged core vertical velocity (w_{co}) and (**b**) cloud-core-shell mixing fraction μ, both averaged over the central 50 % of the cloud layer, for all experiments conducted herein. The color scheme is identical to Fig. 9, and the correlation coefficients for each plotted relation are shown in the lower-right corner of each plot.

300   To investigate the processes regulating w_{co}, we use the core-averaged w equation in CM1 (following de Roode et al., 2012):

$$\left[\frac{Dw}{Dt}\right]_{\mathrm{co}} = -\left[c_{\mathrm{p}}\theta_\rho \frac{\partial \pi'}{\partial z}\right]_{\mathrm{co}} + b_{\mathrm{co}} - \frac{\varepsilon_{\mathrm{w}} w_{\mathrm{co}}^2}{1 - a_{\mathrm{co}}}, \tag{3}$$

where c_{p} is the specific heat of dry air at constant pressure, θ_ρ is the density potential temperature, π is the Exner function and π' its perturbation relative to the horizontal average, ε_{w} is the fractional entrainment rate of w, and the effects of subgrid turbulent mixing are neglected. The dominant terms on the right side of Eq. (3) are the first two (pressure gradient and buoyancy) (e.g., Tang and Kirshbaum, 2020), and we henceforth neglect the entrainment term because it has been found to be small (e.g., de Roode et al., 2012).

The expected tendency for cloud-layer shear to enhance the adverse vertical perturbation pressure gradient (or $\mathrm{VPPG}_{\mathrm{co}}$) is reproduced in the CL-SHR experiments, but more strongly so in BOMEX than in ARM-SGP (Figs. 9a, c). To interpret why the BOMEX $\mathrm{VPPG}_{\mathrm{co}}$ is more sensitive to the shear, we use the linear theory of shallow convection in Kirshbaum and Straub (2019), who found that the VPPG-induced updraft suppression depends on the cloud width and layer depth (Appendix A). Because narrower and taller clouds are more tilted by the shear than are wider, shallower clouds, they experience a larger $\mathrm{VPPG}_{\mathrm{co}}$ enhancement with increasing shear. The convective growth rate (σ) calculated using the linear theory for both BOMEX and ARM-SGP is more than halved between the CTRL and S9 cases. The marginal reduction owing to the shear may be measured by the ratio of the growth rates in the S9 and CTRL cases, which is smaller for BOMEX (0.33) than for ARM-SGP (0.45), suggesting greater shear-induced suppression for the narrower clouds in BOMEX. Although these differences in σ are not dramatic, they lead to large differences over time because σ is an exponential argument. For example, over a 10-min period

representing the growing phase of a shallow cumulus (e.g., Rauber et al., 2007), the theoretical shear-induced reduction in w becomes twice as large in BOMEX as in ARM-SGP.

The second important term in Eq. (3) is the cloud-core buoyancy, which is highly sensitive to lateral entrainment (e.g., Kirshbaum and Grant, 2012). Neggers et al. (2002) argued that a faster ascending core experiences less entrainment and, hence, maintains larger buoyancy, which further accelerates its ascent. Although b_{co} and w_{co} both decrease with increasing vertical shear in the CL-SHR experiments, the b_{co} sensitivity is comparatively modest and of similar strength in BOMEX and ARM-SGP (Figs. 9b, d). Thus, while both of the dominant terms in Eq. (3) tend to suppress w_{co} in shear flows, the VPPG$_{co}$ term largely explains the contrasting sensitivities of w_{co} to cloud-layer shear in BOMEX and ARM-SGP (Figs. 8a-b).

The adverse VPPG$_{co}$ also strengthens with increasing U across the BOMEX WIND and SCL-SHR experiments, at a magnitude comparable to that in the CL-SHR experiments (Figs. 9e, i). This result contrasts sharply with the minimal corresponding variations in ARM-SGP (Figs. 9g, k). Given that the VPPG$_{co}$ sensitivity in CL-SHR was attributed to the prescribed cloud-layer shear, it is fair to wonder if the VPPG$_{co}$ sensitivity in BOMEX is owing to the strong lower-cloud-layer shear that develops in the WIND and SCL-SHR suites (Figs. 2a-d). While this shear likely plays an important role in enhancing the VPPG$_{co}$ in the lower cloud layer, it gradually decays with height above cloud base. However, the VPPG$_{co}$ sensitivity extends throughout the cloud layer, suggesting that the lower-cloud-layer shear is not the sole cause.

Another mechanism behind the VPPG$_{co}$ sensitivities in the BOMEX WIND and SCL-SHR experiments is the associated sensitivity of b_{co} to the background winds (Figs. 9f, j). In both sets of experiments, the maximum b_{co} increases with U. To relate this sensitivity to VPPG$_{co}$, we turn to the diagnostic decomposition of the Boussinesq pressure equation (e.g., Markowski and Richardson, 2010), which may be written

$$c_{p}\theta_{\rho 0}\nabla^{2}\pi' = \underbrace{-\nabla\cdot(\mathbf{u}\cdot\nabla)\mathbf{u}}_{\nabla^{2}p'_{d}} + \underbrace{\frac{\partial b}{\partial z}}_{\nabla^{2}p'_{b}} , \tag{4}$$

where $\theta_{\rho 0}$ is a reference value of θ_{ρ}, $\mathbf{u} = (u, v, w)$, and p'_{b} and p'_{d} denote the buoyancy and dynamic pressure perturbation components, respectively. Away from solid boundaries, the above may be roughly simplified as

$$\pi' \propto -\nabla^{2}p'_{d} - \frac{\partial b}{\partial z} . \tag{5}$$

Neglecting the impacts of the p'_{d} term, larger vertical gradients in b_{co} are associated with larger adverse VPPG$_{co}$, with lower π' below the level of maximum buoyancy and higher π' above it. This implies that the stronger VPPG$_{co}$ sensitivity in the BOMEX WIND and SCL-SHR experiments (relative to the corresponding ARM-SGP experiments) is, in part, associated with the larger b_{co} that develops at larger U. The cause of this wind-induced increase in b_{co} is examined in Sect. 4.2.

The sensitivities of w_{co} in the WIND and SCL-SHR experiments thus appear to be driven by variations in both the VPPG$_{co}$ and b_{co} terms in Eq. (3). While VPPG$_{co}$ exhibits a comparable decrease with increasing U as in the CL-SHR experiments, offsetting variations in b_{co} lead to a muted sensitivity of w_{co} (Figs. 9e, f, i, j and Figs. 8c, e). The sensitivities of both w_{co} and ε in these experiments are much stronger in BOMEX than in ARM-SGP. Unlike in the CL-SHR experiments, these differences cannot be attributed to differential effects on vertical shear on cloud tilting because the cloud-layer shear is too weak. A physical explanation for this behavior is thus required, and one will be provided in Sect. 4.2.

4.2 Properties of entrained air

The analysis in Sect. 4.1 showed that w_{co} often correlates negatively with ε, which may be explained by the role of w_{co} in regulating the time scale over which ascending thermals are exposed to environmental air. However, the fact that w_{co} did not exclusively control ε (Fig. 10a) suggests that other factors are needed to explain the ε sensitivities. One such factor is the nature of the entrained air in the core shell. As the fraction of environmental air within the shell decreases, it becomes less efficient at diluting the cloud core, for all else being equal. Following Hannah (2017), we assume that entrained air is drawn from the cloud-core shell. At each vertical level, this shell is defined following Dawe and Austin (2011) as all non-core grid points immediately adjacent to core points, whether they are saturated or not. We further assume that core-shell air can be expressed as a linear mixture of core and environmental air at that level. Any conserved variable (e.g., the total water specific humidity, s_{t}) may thus be written

$$(s_{\mathrm{t}})_{\mathrm{sh}} = \mu(s_{\mathrm{t}})_{\mathrm{co}} + (1-\mu)(s_{\mathrm{t}})_{\mathrm{en}}, \tag{6}$$

where "en" and "sh" respectively denote the environment and cloud-core shell and μ is the mixing fraction, or the fraction of cloud-core air within the cloud-core shell. Over all the simulations conducted herein, ε tends to increase with μ^{-1}, with a good correlation between them (Fig. 10b).

For the CTRL simulations, the cloud-layer-averaged μ is 0.53 for BOMEX and 0.70 for ARM-SGP (Fig. 11a). Thus, a given entrainment flux yields less core dilution in ARM-SGP than in BOMEX. The imposed cloud-layer vertical wind shear in the CL-SHR experiments has a negligible effect on μ in ARM-SGP, with a marginal increase of only 0.5 % between the CTRL and S9 experiments. In contrast, BOMEX shows a more substantial 15 % corresponding increase (0.61), indicating a shift toward less dilute cloud-core shells. Despite the stronger increase of μ in BOMEX across the CL-SHR experiments, μ is always larger in ARM-SGP (Fig. 11a). This effect, along with the universally larger w_{co} in ARM-SGP, largely explains why ε is always smaller in ARM-SGP than in BOMEX.
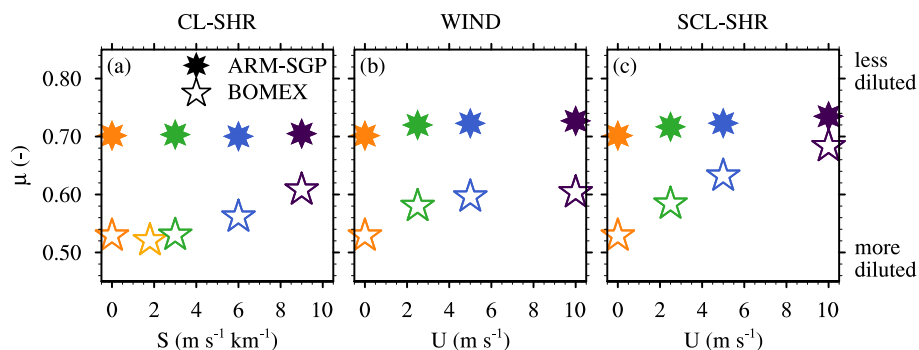
Figure 11. Mixing fraction μ for entraining nearest-neighbor adjacent core-exterior grid points for (**a**) the CL-SHR, (**b**) the WIND, and (**c**) the SCL-SHR experiments. The color scheme is identical to Fig. 9.

The BOMEX core shells also become less diluted as U is increased in the WIND simulations, with μ increasing from 0.53 in CTRL to 0.60 in U10 (Fig. 11b). This increase is the largest between the CTRL and U2.5 cases and ultimately levels off between the U5 and U10 cases. A similar lack of sensitivity between the U5 and U10 cases is apparent in the w_{co}, VPPG$_{co}$, b_{co}, and ε profiles (Figs. 8c, 9e-f, and 7a, respectively). As in the CL-SHR experiments, μ varies minimally in the corresponding ARM-SGP experiments, with an increase of only 4 % from CTRL to U10. Whereas the addition of subcloud geostrophic shear in the SCL-SHR experiments has a minimal additional impact on μ in ARM-SGP (Fig. 11c), it leads to a stronger and more systematic increase in μ in BOMEX, to a value of 0.68 in US40. Although the variations in μ across the various suites of simulations are modest, they suffice to explain the notable variations in b_{co} in the BOMEX WIND and SCL-SHR experiments (Figs. 9b, f, and j). This is shown by a simple entraining parcel calculation that explicitly accounts for the cloud-core shell (Appendix B).

What controls the sensitivity of μ in BOMEX to the initial wind profile, and why is this sensitivity lacking in ARM-SGP? These questions are addressed by looking farther afield than just the immediate core-adjacent grid points that constitute the cloud-core shell. To this end, we define a wider region surrounding the core as the "cloud-core margin", over which μ falls from its in-core values of approximately unity down to 0.5. This margin, which encapsulates the cloud-core shell, can be viewed as a finite-width halo of mixed air surrounding the core that shields it from pure environmental air. The width of this margin is henceforth denoted R_m.

At each vertical level, we define R_m as the distance from the core edge to the nearest grid point where $\mu \leq 0.5$. This quantity is evaluated separately along both coordinate axes to compare the along- and cross-wind directions. The values of R_m thus presented are averaged over the central 50 % of the cloud layer (Fig. 12). While R_m is nearly axisymmetric for the CTRL cases (orange markers in Fig. 12), it develops anisotropy in the sensitivity tests. In the BOMEX CL-SHR experiments, R_m grows in all directions but to the largest degree (120 %) on the downshear side of the cloud cores (Fig. 12a). In ARM-SGP, R_m only grows noticeably on the downshear side, by around 50 % (Fig. 12b). The downshear widening of R_m is consistent with the formation of a humid downshear wake (e.g., Heus and Jonker, 2008).

In the BOMEX WIND experiments, R_m again grows in all directions as U is increased (Fig. 12c), but to a slightly lesser degree than in the corresponding CL-SHR experiments. Moreover, the core-margin expansion is maximized on the northern and western flanks of the cores, as opposed to the east side in the CL-SHR experiments, due to the weak east-southerly shear that develops in the lower cloud layer (Figs. 2a-b). For the ARM-SGP WIND experiments, R_m again undergoes less variation than in the corresponding BOMEX experiments, with the largest expansion on the downshear (southeasterly) side of the cores (Fig. 12d). In the SCL-SHR experiments, R_m shows an even stronger sensitivity to U in BOMEX while it remains virtually unchanged from the WIND experiments in ARM-SGP (Figs. 12e-f).

In absolute terms, R_m averaged over all directions is about 60 % smaller in the CTRL BOMEX case than in the CTRL ARM-SGP case (Figs. 13a-c). The cloud cores in BOMEX thus have narrower buffer zones surrounding them, which increases their exposure to environmental air. Wider core margins tend to exhibit larger μ because, as the transition from core to environmental air becomes more gradual, the air immediately adjacent to the core becomes more core-like. For the three sets of experiments, the ARM-SGP R_m is generally less sensitive to changes in the wind profile than the corresponding BOMEX value. Whereas
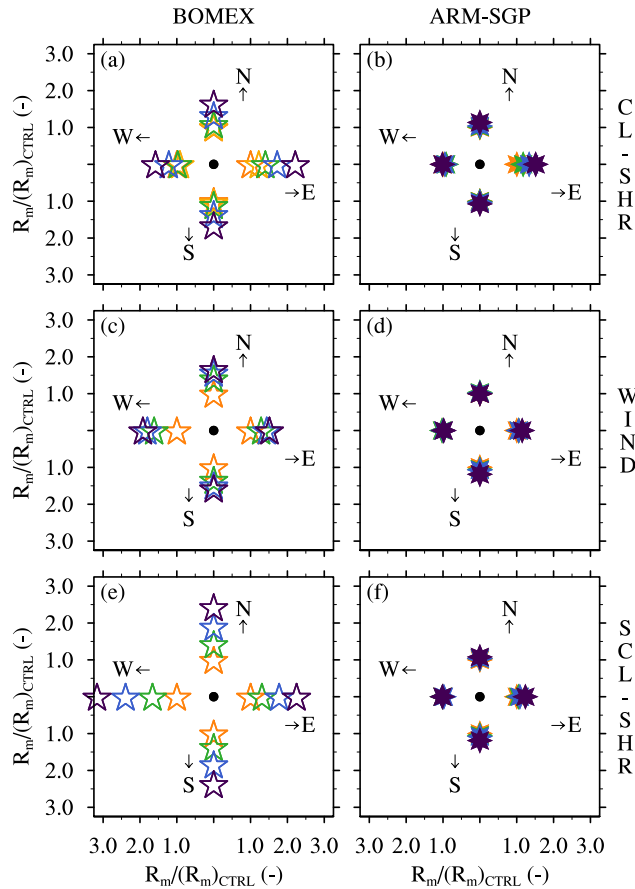
Figure 12. Radius of the cloud-core margin (R_m) averaged over the central 50 % of cloud layer for the different directions normalized by the averaged R_m for the respective CTRL cases for (**a-b**) the CL-SHR, (**c-d**) the WIND, and (**e-f**) the SCL-SHR experiments. Panels (**a**), (**c**) and (**e**) show the BOMEX cases and panels (**b**), (**d**), and (**f**) the ARM-SGP cases. The color scheme is identical to Fig. 9.

the former exhibits a maximum increase of 17 % for the CL-SHR experiments, BOMEX exhibits a maximum increase of 153 % for the SCL-SHR experiments.

In general, R_m correlates well with μ (cf. Figs. 13a-c and Fig. 11), with the lone exception being the ARM-SGP CL-SHR

410 experiments, where a 17 % enhancement in R_m does not coincide with increased μ. We hypothesize that two factors combine to regulate R_m: the turbulence intensity within the cloud margin, which determines the lateral eddy diffusion rate, and w_co, which determines the diffusion time scale. These two effects may be combined into a nondimensional number $r = \mathrm{TKE}_\mathrm{CL}^{1/2}/w_\mathrm{co}$, where TKE_CL is the cloud-layer averaged TKE. Larger r implies increased turbulent diffusion within the core margin, which enhances R_m.

415 For each suite of simulations (e.g., BOMEX WIND), the relative variations in r align well with corresponding variations in R_m (Figs. 13j-l and 13a-c), again with the exception of the ARM-SGP CL-SHR experiments, where r increases more rapidly
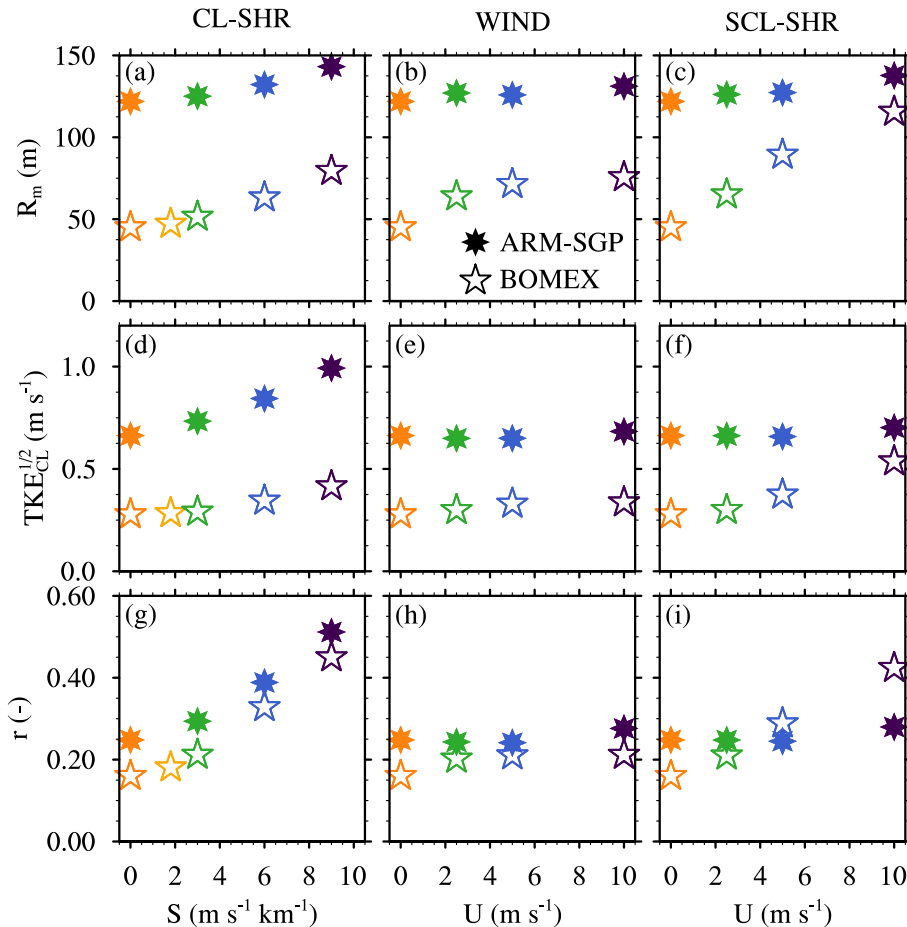
Figure 13. Various properties relevant to the (**a-c**) the cloud-core margin width averaged over all directions and the central 50 % of the cloud layer (R_m), (**d-f**) the square root of cloud-layer TKE ($\mathrm{TKE}_\mathrm{CL}^{1/2}$), and (**g-i**) $r = \mathrm{TKE}_\mathrm{CL}^{1/2}/w_\mathrm{co}$. Panels (**a**), (**d**), and (**g**) show the CL-SHR, panels (**b**), (**e**), and (**h**) the WIND, and (**c**), (**f**), and (**i**) the SCL-SHR experiments. The color scheme is identical to Fig. 9.

than R_m across the suite of experiments. Note that variations in r between different suites of experiments (e.g., BOMEX CL-SHR versus ARM-SGP CL-SHR) must be multiplied by a relevant length scale to permit direct comparison to the dimensional R_m. The most appropriate length scale is the mean core radius or the length scale of maximum TKE_CL, both of which are about twice as large in ARM-SGP than in BOMEX (Sect. 3). With this factor taken into account, the variations in r become even more consistent with those in R_m.

Using r to help interpret variations in R_m, we attribute the increased R_m in the CL-SHR experiments to a joint decrease in w_co (Figs. 8a-b) and an increase in TKE_CL (Figs. 8d). The w_co effect was explained in detail in Sect. 4.1, and the TKE effect is a direct result of enhanced turbulent shear production. Although the same basic trend holds in BOMEX and ARM-SGP, the sensitivity is stronger in BOMEX due to its stronger shear-induced suppression of w_co, as well as the minimal changes

in μ across the ARM-SGP simulations (Fig. 11a). These results suggest that w_{co} has competing effects on cloud dilution. A decreased w_{co} lengthens the exposure of cloud cores to their environment, but it also favors a wider core margin that better shields the cores from their environment. In CL-SHR, the former effect dominates over the latter, and ε increases.

The r and R_{m} trends across the WIND experiments differ between BOMEX and ARM-SGP, with ARM-SGP showing minimal changes due to the joint invariance of w_{co} and $\mathrm{TKE_{CL}}$ (Figs. 8d and 13e). In BOMEX, by contrast, w_{co} decreases slightly as $\mathrm{TKE_{CL}}$ increases across the WIND experiments (Figs. 8c and 13e), leading to a substantial increase in r and R_{m} (Figs. 13b, h). These trends are amplified in the SCL-SHR experiments (Figs 13c, i), where r and R_{m} rapidly increase owing to a large decrease in w_{co} combined with a large increase in $\mathrm{TKE_{CL}}$ (Figs. 8e and 13j).

To explain the mechanisms causing the variations in R_{m} across the WIND experiments, the subcloud dynamics must be considered. Due to surface friction, larger U leads to enhanced subcloud vertical shear, which gives rise to increased subcloud TKE and length scales. The larger subcloud thermals, in turn, initiate larger clouds, and R_{LFC} increases by 73 % and 13 % across the BOMEX and ARM-SGP experiments, respectively (Figs. 6e-f). The fractional increases in low-level TKE in Figs. 14a-b are also much larger in BOMEX (50 %) than in ARM-SGP (10–20 %), due to the larger baseline TKE in the strongly heated ARM-SGP case. Vertical transport of this enhanced subcloud TKE, combined with the weak shear that forms in the lower cloud layer, leads to enhanced $\mathrm{TKE_{CL}}$, particularly in BOMEX (Fig. 13e). Correspondingly, r and R_{LFC} increase by a larger fraction in BOMEX than in ARM-SGP (Fig. 13h), a trend that strengthens in the SCL-SHR experiments (Figs. 14a-b).

The two competing impacts of reduced w_{co} are again active in the WIND experiments, but in this case ε decreases with increasing U (Fig. 7a), suggesting that the buffering effect of the wider core margin dominates over the diluting effect of a longer core-exposure time scale. For ARM-SGP, on the other hand, the changes in w_{co} and μ are both small, leading to only a minimal decrease in ε (Fig. 7b). The SCL-SHR experiments again exhibit similar trends in ε as those in the WIND experiments (Figs. 7c-d). In BOMEX SCL-SHR, larger increases in subcloud TKE and $\mathrm{TKE_{CL}}$ lead to even larger increases in μ. However, the stronger corresponding reduction in w_{co} counters this effect to yield a similar ε trend as that in BOMEX WIND.

Returning to the CL-SHR experiments, the positive sensitivity of ε to vertical wind shear differs from Lin (1999), Brown (1999), and Helfer et al. (2020), who all found minimal corresponding sensitivities. These differences may be explained by a combination of factors. Because Lin (1999) evaluated ε based on the vertical mass flux profile alone, they neglected the important role of detrainment in shaping that profile. Although Brown (1999) calculated ε using a rigorous method (SC95), they used geostrophic shear profiles extending over both the subcloud and cloud layers. Given that cloud-layer shear and subcloud shear have opposing effects on ε, it is possible that these two effects largely cancelled. Similar to Brown (1999), Helfer et al. (2020) used vertically constant shear profiles in their LES study. Furthermore, they employed the simpler "bulk-plume" method to ε, which neglects two of the terms in the SC95 formulation (Betts, 1975). More difficult to reconcile is the recent observational finding from Kirshbaum and Lamer (2021) that retrieved ε does not vary systematically with cloud-layer shear, in oceanic or continental locations. It is possible that offsetting effects between subcloud and cloud-layer shear also occur in reality, and/or that the differences between geostrophic winds (used herein) and full winds (used in Kirshbaum and Lamer, 2021) could explain these differences.
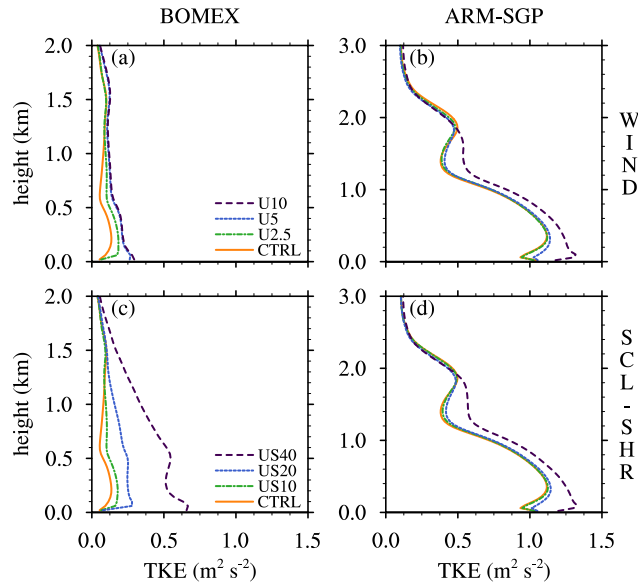
Figure 14. Vertical profiles of domain-averaged TKE for (**a-b**) the WIND and (**c-d**) the SCL-SHR experiments. Panels (**a**) and (**c**) show the BOMEX cases and the panels (**b**) and (**d**) the ARM-SGP cases.

4.3 Empirical Relationship

Following from the results presented above, we have developed an empirical relationship for ε that takes the two key controls on cloud dilution identified herein into account. These controls are the "core exposure effect" regulated by w_{co} and the "core-shell dilution effect" (i.e. the amount of dilution per unit of entrainment) determined by μ. As seen in Fig. 10, these two quantities vary roughly inversely with ε, which guides the form of the empirical function. Based on all the experiments conducted herein, we propose the following empirical function:

$$\varepsilon_{\mathrm{DKK}} = w_{\mathrm{co}}^{\alpha}\mu^{\beta} + \gamma,\tag{7}$$

with $\alpha = -1.14$, $\beta = -1.84$, and $\gamma = -0.2$. Calculated for CL-SHR, WIND, and SCL-SHR experiments, $\varepsilon_{\mathrm{DKK}}$ approximates the simulated ε very well (R=0.99; Fig. 15). Thus, w_{co} and μ can explain nearly all variation in ε found in this study. However, w_{co}, μ, and ε are highly inter-dependent, in that w_{co} and μ both regulate ε and are influenced by it. In addition to ε, w_{co} and μ also depend on other processes, namely the vertical perturbation pressure gradient and buoyancy for w_{co} and cloud-layer turbulence and w_{co} for μ. The interrelationship of w_{co}, μ, and ε is complicated and demands further analysis. However, such an investigation is beyond the scope of this study and is deferred to future work.
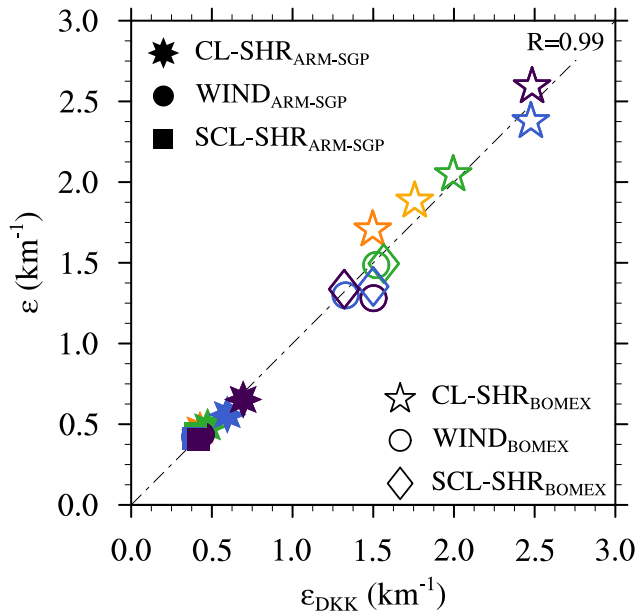
Figure 15. Relation of simulated dilution rate (ε) and dilution rates ($\varepsilon_{\mathrm{DKK}}$) obtained using the empirical formulation in Eq. (7).

5 Conclusions

In this second part of a two-part study on the environmental controls on shallow-cumulus dilution, the impacts of variations in the geostrophic wind profile on cloud dilution have been investigated. To this end, LES experiments were conducted that systematically varied the cloud-layer vertical shear (CL-SHR; from 0 to 9 m s^{-1} km^{-1}), the background wind speed (WIND; from 0 to 10 m s^{-1}), and the subcloud (0-250 m above ground level) vertical shear (SCL-SHR; from 0 to 40 m s^{-1} km^{-1}). To consider different shallow-cumulus manifestations observed in reality, these tests were run on both a quasi-statistically steady maritime, trade-wind flow (BOMEX) and a diurnally forced continental flow (ARM-SGP).

Altogether, the experiments suggested that two basic factors control the sensitivity of the simulated cloud-core dilution rate (ε) to the imposed winds: the time scale over which the ascending cloud cores are exposed to environmental air, and the mixing fraction (μ, representing the fraction of cloud-core air within the mixture) of the "shell" immediately outside to the core, from which entrained air is drawn. The first effect, which we call the "core exposure effect", is directly controlled by the cloud-core vertical velocity w_{co} and induces an inverse relationship between w_{co} and ε (e.g., Neggers et al., 2002). The second effect, called the "core-shell dilution effect", is largely controlled by the width of the buffer zone between core and environmental air. Larger widths exhibit more gradual transitions from core to environmental air, which give larger μ in the grid points immediately adjacent to the core. These widths were largely controlled by the ratio of the square root of core-layer TKE to w_{co}.

The core-exposure and core-shell-dilution effects both depend inversely on w_{co} and tend to mutually offset. For example, a decrease in w_{co} increases the core-exposure time scale, which tends to enhance dilution, while also increasing the core-shell-

mixing time scale, which tends to weaken dilution by increasing μ. In the CL-SHR experiments, the vertical shear induced a large (up to 50 %) decrease in w_{co}, owing to enhanced vertical perturbation pressure gradients suppressing the updrafts. As a result, the core-exposure effect tended to enhance dilution while the core-shell dilution effect tended to weaken it. In this case, the core-exposure effect dominated, leading to an increase in ε (by up to 50 %) under stronger cloud-layer vertical shear.

In contrast, for the WIND and SCL-SHR experiments, the main sensitivities of ε were traced to subcloud, rather than cloud-layer, processes. The strong near-surface shears in both cases (either prescribed or induced by surface drag) increased the subcloud TKE, which extended into the cloud layer. As a result, the mixing rate within the cloud shells increased to give larger μ, which favored a buffering of the cloud cores. Although w_{co} also exhibited a small decrease with increasing winds, thereby activating the core-exposure effect, the core-shell-dilution effect was dominant, leading to decreased ε (by up to 25 %) under increasing geostrophic winds (and subcloud shears). Thus, the effect of vertical shear on ε depends on the layer where the shear is applied; cloud-layer shear enhances cloud dilution while subcloud shear decreases it.

The maritime BOMEX simulations were generally more sensitive to changes in the geostrophic wind profile than the ARM-SGP simulations, for two main reasons. Firstly, as found in the CL-SHR experiments, the weaker sensible heating over the ocean supports shallower subcloud layers with smaller-scale subcloud updrafts, which, in turn, initiate smaller cumuli. These cumuli were more susceptible to shear-induced tilting, and thus were more suppressed by the shear than the wider cumuli in ARM-SGP. Secondly, as found in the WIND and SCL-SHR experiments, the subcloud TKE was more sensitive to low-level shear in BOMEX than in ARM-SGP, mainly because the weaker surface heating in BOMEX yielded a lower baseline TKE. Extension of this enhanced TKE into the cloud layer widened the transition zones between the cores and their environment, thus inducing a buffering effect. Because the low-level TKE was only marginally enhanced by the subcloud shear in the corresponding ARM-SGP simulations, these cases were nearly insensitive to changes in the geostrophic wind profile.

The robust positive sensitivity of ε to the cloud-layer shear in the CL-SHR differs from the findings of previous LES studies (Lin, 1999; Brown, 1999; Helfer et al., 2020) and observational ε retrievals (Kirshbaum and Lamer, 2021). While the former discrepancies can be explained by key differences in model initialization or ε diagnoses, the latter is more concerning and merits future investigation. Such analysis would need to include the use of instrument simulators to ensure that both observed and simulated ε are calculated for comparable subsets of shallow cumuli and the comparison is not compromised by the difficulty of observationally detecting clouds with small LWC. In contrast, the weakening of ε with increasing background winds in the BOMEX WIND and SCL-SHR is consistent with Kirshbaum and Lamer (2021), who found a robust inverse relationship between U and ε in the oceanic Eastern North Atlantic ARM site in the Azores. In a followup study, it would be interesting to investigate the cloud-core margin (R_m) in observations and whether it can be related to reflectivity variability at each level within the cloud.

Appendix A: Linear theory of shallow convection

Kirshbaum and Straub (2019) have used the linear theory for statically unstable cloud layers with background vertical wind shear to examine the impact of vertical wind shear on shallow convection. This model is used to help interpret the stronger

shear-induced suppression of cumuli in BOMEX than in ARM-SGP. In the linear theory, the convective growth rate (σ) is evaluated as a function of the nondimensional horizontal wavenumber κH, where $\kappa = 2\pi/\lambda$ is the 2D horizontal wavenumber and H is the depth of moist-unstable cloud layer, the latter characterized by negative Brunt-Väisälä frequency (N_m^2; Durran and Klemp, 1982).

To determine the applicability of the linear theory to our simulations, we compare the linear-predicted updraft suppression between the CTRL and S9 simulations for both BOMEX and ARM-SGP. For this analysis, κ is assigned as the wavenumber of the spectral peak of the cloud-layer-averaged Fourier kinetic energy spectrum, H is the depth of the layer over which $N_m^2 < 0$ (assuming saturated flow), and N_m^2 is averaged over H. A comparison of these quantities for the CTRL cases indicates smaller κ (and hence larger horizontal scales) and a shallower unstable layer depth for ARM-SGP (Table A1), yielding smaller cloud aspect ratios. Substituting these values, along with the zonal vertical shear magnitude, into the linear model of Kirshbaum and Straub (2019), we obtain the σ values in Table A1.

Table A1. Summary of linear theory analysis. All symbols are defined in the text.

	κ (km^{-1})	H (km)	N_m^2 (10^{-5} s^{-2})	σ (10^{-2} s^{-1})
BOMEX-CTRL	0.74	0.8	-5.0	0.64
BOMEX-S9	0.74	0.8	-5.0	0.21
ARM-SGP-CTRL	0.44	0.6	-6.0	0.58
ARM-SGP-S9	0.44	0.6	-6.0	0.26

Appendix B: Parcel model

To show that the modest changes in μ across the WIND simulations (Fig. 11) suffice to explain the corresponding variations in b_{co} in Fig. 9, we use a simple entraining parcel model similar to that developed by Hannah (2017) to illustrate the effect of increased μ and b_{co}. This model draws a mean-layer (0-500 m) parcel from the initial BOMEX sounding and adiabatically lifts it to the base of the trade-wind inversion at 1.5 km. Above the LFC, it ingests surrounding air at a fixed rate of ε_p, where "p" denotes the parcel. Rather than entraining pure environmental air, the parcel entrains a mixture of core and environmental air from the core shell. Assuming a statistically steady cloud field, and that the parcel equivalent potential temperature (θ_e) is conserved with height except for this mixing, the dilution may be estimated using

$$\frac{\partial (\theta_e)_p}{\partial z} = -\varepsilon_p \left((\theta_e)_p - (\theta_e)_{sh} \right). \tag{B1}$$

The shell properties are related to those of the environment and parcel by μ:

$$(\theta_e)_{sh} = \mu (\theta_e)_p + (1 - \mu)(\theta_e)_{en}. \tag{B2}$$

Combining Eq. (B1) and Eq. (B2), we obtain

$$\frac{\partial (\theta_e)_p}{\partial z} = -\varepsilon_p (1 - \mu) \left((\theta_e)_p - (\theta_e)_{en} \right) . \tag{B3}$$

We solve Eq. (B3) numerically to obtain $(\theta_e)_p$, and retrieve the parcel properties from it to evaluate b_p.

The factor $\varepsilon_p (1 - \mu)$ in Eq. (B3) indicates that, for $\mu > 0$, the core shell effectively weakens the cloud dilution from a given entrainment rate ε_p, and the strength of this effect increases with ε_p. Because the ε formulation in SC95 does not explicitly account for the impacts of the core shell, ε_p must exceed the SC95-calculated ε to realize the same amount of core dilution. Given that $\varepsilon \approx 1.5$ km^{-1} and $\mu \approx 0.6$ in BOMEX CTRL, we set $\varepsilon_p = 2.5$ km^{-1} to yield similar cloud dilution as that in the BOMEX simulations, thus facilitating a more direct comparison. This enhanced value of ε_p is similar in magnitude to the LES-based direct entrainment rates reported in the literature (e.g, Romps, 2010; Dawe and Austin, 2011).

Figure B1 compares the parcel-model-derived b_p for the BOMEX case for $\mu = 0.53$ and $\mu = 0.60$, matching the range found across the WIND simulations. For the chosen ε_p, the magnitudes and sensitivities b_p are very similar, if not larger, to those found in the corresponding BOMEX WIND simulations (Fig. 9f). Thus, the variations in b_{co} in the BOMEX WIND and SCL-SHR sensitivity tests can largely be explained by corresponding variations in μ. Similarly, the minimal variations in b_{co} among the corresponding ARM-SGP experiments are consistent with their minimal μ sensitivities. This analysis does not carry over to the CL-SHR experiments because the variations in μ coincide with large variations in w_{co}, which may also impact b_{co}.

Code and data availability. The Bryan Cloud Model (CM1) is available under http://www2.mmm.ucar.edu/people/bryan/cm1/ (last access: 10 September 2020). Simulated data and analysis scripts as well as other supplementary information that may be useful for reproducing the author's work are archived by the Department of Atmospheric and Oceanic Sciences (McGill University) under https://aos.meteo.mcgill.ca/ (last access: 10 August 2021). The username and password can be obtained by contacting sonja.drueke@mail.mcgill.ca.

Author contributions. S.D. and D.J.K. developed the scientific question, and S.D. conducted the simulations and carried out the analysis under the supervision of D.J.K. and co-supervision of P.K. S.D. prepared the paper with contributions from D.J.K. and P.K.

Competing interests. The authors declare that they have no conflict of interest.

Acknowledgements. Research funding was provided from the Natural Sciences and Engineering Research Council (NSERC) Grant NSERC/ RGPIN 418372-17 and the US Department of Energy Atmospheric System Research (DOE–ASR) Program under contract DE-SC0020083. P.K. was supported by the US Department of Energy (DOE) Atmospheric System Research Program under contract DE-SC0012704. The numerical simulations were performed on the Guillimin supercomputer at McGill University and Béluga supercomputer at the École de technologie supérieure, both under the auspices of Calcul Québec and Compute Canada.
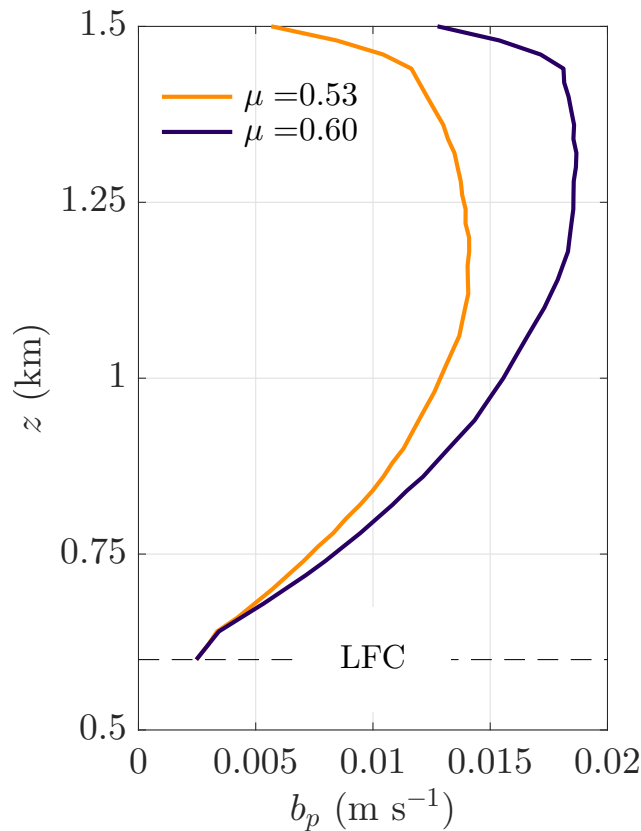
Figure B1. Sensitivity of entraining-parcel-model buoyancy (b_p) to core-shell mixing fraction (μ) for the initial BOMEX sounding, assuming a vertically constant shell-entrainment rate of $\varepsilon_\mathrm{p} = 2.5$ km^{-1}.

References

Asai, T.: Cumulus Convection in the Atmosphere with Vertical Wind Shear: Numerical Experiment, J. Meteor. Soc. Japan, 42, 245–259,
575   https://doi.org/10.2151/jmsj1923.42.4_245, 1964.

Bera, S. and Prabha, T. V.: Parameterization of Entrainment Rate and Mass Flux in Continental Cumulus Clouds: Inference From Large Eddy
Simulation, J. Geophys. Res. Atmos., 124, 13 127–13 139, https://doi.org/10.1029/2018JD031078, 2019.

Betts, A. K.: Parametric Interpretation of Trade-Wind Cumulus Budget Studies, J. Atmos. Sci., 32, 1934–1945, https://doi.org/10.1175/1520-
0469(1975)032<1934:PIOTWC>2.0.CO;2, 1975.

580   Brown, A. R.: Large-Eddy Simulation and Parametrization of the Effects of Shear on Shallow Cumulus Convection, Bound.-Layer Meteor.,
91, 65–80, https://doi.org/10.1023/A:1001836612775, 1999.

Brown, A. R., Cederwall, R. T., Chlond, A., Duynkerke, P. G., Golaz, J.-C., Khairoutdinov, J. M., Lewellen, D. C., Lock, A. P., Macvean,
M. K., Moeng, C.-H., Neggers, R. A. J., Siebesma, A. P., and Stevens, B.: Large-eddy simulation of the diurnal cycle of shallow cumulus
convection over land, Quart. J. Roy. Meteor. Soc., 128, 1075–1094, https://doi.org/10.1256/003590002320373210, 2002.

585   Bryan, G. H. and Fritsch, J. M.: A Benchmark Simulation for Moist Nonhydrostatic Numerical Models, Mon. Wea. Rev., 130, 2917–2928, https://doi.org/10.1175/1520-0493(2002)130<2917:ABSFMN>2.0.CO;2, 2002.

Dawe, J. T. and Austin, P. H.: Interpolation of LES Cloud Surfaces for Use in Direct Calculations of Entrainment and Detrainment, Mon. Wea. Rev., 139, 444–456, https://doi.org/10.1175/2010MWR3473.1, 2011.

de Roode, S. R., Siebesma, A. P., Jonker, H. J. J., and de Voogd, Y.: Parameterization of the vertical velocity equation for shallow cumulus

590   clouds, Mon. Wea. Rev., 140, 2424–2436, https://doi.org/10.1175/MWR-D-11-00277.1, 2012.

de Rooy, W. C., Bechtold, P., Fröhlich, K., Hohenegger, C., Jonker, H., Mironov, D., Siebesma, A. P., Teixeira, K., and Yano, J.-I.: Entrainment and detrainment in cumulus convection: an overview, Quart. J. Roy. Meteor. Soc., 139, 1–19, https://doi.org/10.1002/qj.1959, 2013.

Deardorff, J. W.: Numerical Investigation of Neutral and Unstable Planetary Boundary Layers, J. Atmos. Sci., 29, 91–115, https://doi.org/10.1175/1520-0469(1972)029<0091:NIONAU>2.0.CO;2, 1972.

595   Del Genio, A. D.: Representing the Sensitivity of Convective Cloud Systems to Tropospheric Humidity in General Circulation Models, Surv. Geophys., 33, 637–656, https://doi.org/10.1007/s10712-011-9148-9, 2012.

Derbyshire, S. H., Beau, I., Bechtold, P., Grandpeix, J.-Y., Piriou, J.-M., Redelsperger, J. L., and Soares, P. M. M.: Sensitivity of moist convection to environmental humidity, Quart. J. Roy. Meteor. Soc., 130, 3055–3079, https://doi.org/10.1256/qj.03.130, 2004.

Drueke, S., Kirshbaum, D. J., and Kollias, P.: Evaluation of Shallow-Cumulus Entrainment Rate Retrievals Using Large-Eddy Simulation, J.

600   Geophys. Res. Atmos., 124, 9624–9643, https://doi.org/10.1029/2019JD030889, 2019.

Drueke, S., Kirshbaum, D. J., and Kollias, P.: Environmental sensitivities of shallow-cumulus dilution. Part 1: Selected thermodynamic conditions, Atmos. Chem. Phys., 20, 13 217–13 239, https://doi.org/10.5194/acp-20-13217-2020, 2020.

Durran, D. R. and Klemp, J. B.: On the effects of moisture on the Brunt-Väisälä frequency, J. Atmos. Sci., 39, 2152–2158, https://doi.org/10.1175/MWR-D-17-0056.1, 1982.

605   Endo, S., Zhang, D., Vogelmann, A. M., Kollias, P., Lamer, K., Oue, M., Xiao, H., Gustafson Jr., W. I., and Romps, D. M.: Reconciling differences between large-eddy simulations and Doppler lidar observations of continental shallow cumulus cloud-base vertical velocity, Geophys. Res. Lett., 46, 11 539– 11 547, https://doi.org/10.1029/2019GL084893, 2019.

Gerber, H. E., Frick, G. M., Jensen, J. B., and Hudson, J. G.: Entrainment, Mixing and Microphysics in Trade-Wind Cumulus, J. Meteor. Soc. Japan, 86A, 87–106, https://doi.org/10.2151/jmsj.86A.87, 2008.

610   Gibert, F., Arnault, N., Cuesta, J., Plougonven, R., and Flamant, P. H.: Internal gravity waves convectively forced in the atmospheric residual layer during the morning transition, Quart. J. Roy. Meteor. Soc., 137, 1610–1624, https://doi.org/10.1002/qj.836, 2011.

Hannah, W. M.: Entrainment versus Dilution in Tropical Deep Convection, J. Atmos. Sci., 74, 3725–3747, https://doi.org/10.1175/JAS-D-16-0169.1, 2017.

Helfer, K. C., Nuijens, L., de Roode, S. R., and Siebesma, A. P.: How Wind Shear Affects Trade-wind Cumulus Convection, J. Adv. Model.

615   Earth Syst., 12, e2020MS002 183, https://doi.org/10.1029/2020MS002183, 2020.

Heus, T. and Jonker, H. J. J.: Subsiding Shells around Shallow Cumulus Clouds, J. Atmos. Sci., 65, 1003–1018, https://doi.org/10.1175/2007JAS2322.1, 2008.

Heymsfield, A. J., Johnson, P. N., and Dye, J. E.: Observations of Moist Adiabatic Ascent in Northeast Colorado Cumulus Congestus Clouds, J. Atmos. Sci., 35, 1689–1703, https://doi.org/10.1175/1520-0469(1978)035<1689:OOMAAI>2.0.CO;2, 1978.

620   Houghton, H. G. and Cramer, H. E.: A Theory of Entrainment in Convective Currents, J. Meteor., 8, 95–102, https://doi.org/10.1175/1520-0469(1951)008<0095:ATOEIC>2.0.CO;2, 1951.

Khairoutdinov, M. F. and Randall, D. A.: High-Resolution Simulation of Shallow-to-Deep Convection Transition over Land, J. Atmos. Sci., 63, 3421–3436, https://doi.org/10.1175/JAS3810.1, 2006.

Kirshbaum, D. J.: Numerical Simulations of Orographic Convection Across Multiple Gray Zones, J. Atmos. Sci., 77, 3301 – 3320, https://doi.org/10.1175/JAS-D-20-0035.1, 2020.

Kirshbaum, D. J. and Grant, A. L. M.: Invigoration of cumulus cloud fields by mesoscale ascent, Quart. J. Roy. Meteor. Soc., 138, 2136–2150, https://doi.org/10.1002/qj.1954, 2012.

Kirshbaum, D. J. and Lamer, K.: Climatological sensitivities of shallow-cumulus bulk entrainment in continental and oceanic locations, J. Atmos. Sci., submitted, 2021.

Kirshbaum, D. J. and Straub, D. N.: Linear theory of shallow convection in deep, vertically sheared atmospheres, Quart. J. Roy. Meteor. Soc., 145, 3129–3147, https://doi.org/10.1002/qj.3609, 2019.

Krueger, S. K.: Fine-scale modeling of entrainment and mixing of cloudy and clear air, Proc. ICCP 2008, pp. Cancun (Mexico), July 7–11, 2008.

Lamer, K., Kollias, P., and Nuijens, L.: Observations of the variability of shallow trade wind cumulus cloudiness and mass flux, J. Geophys. Res. Atmos., 120, 6161– 6178, https://doi.org/10.1002/2014JD022950, 2015.

Lin, C.: Some Bulk Properties of Cumulus Ensembles Simulated by a Cloud-Resolving Model. Part II: Entrainment Profiles, J. Atmos. Sci., 56, 3736–3748, https://doi.org/10.1175/1520-0469(1999)056<3736:SBPOCE>2.0.CO;2, 1999.

Lu, C., Niu, S., Liu, Y., and Vogelmann, A. M.: Empirical relationship between entrainment rate and microphysics in cumulus clouds, Geophys. Res. Lett., 40, 2333–2338, https://doi.org/10.1002/grl.50445, 2013.

Lu, C., Sun, C., Liu, Y., Zhang, G., Lin, Y., Gao, W., Niu, S., Yin, Y., Qiu, Y., and Jin, L.: Observational Relationship Between Entrainment Rate Environmental Relative Humidity and Implications for Convection Parameterization, Geophys. Res. Lett., 45, 13,495–13,504, https://doi.org/10.1029/2018GL080264, 2018.

Malkus, J. S.: The slopes of cumulus clouds in relation to external wind shear, Quart. J. Roy. Meteor. Soc., 78, 530–542, https://doi.org/10.1002/qj.49707833804, 1952.

Markowski, P. and Richardson, Y.: Mesoscale Meteorology in Midlatitudes, Wiley, 2010.

McMichael, L. A., Yang, F., Marke, T., Löhnert, U., Mechem, D. B., Vogelmann, A. M., Sanchez, K., Tuononen, M., and Schween, J. H.: Characterizing subsiding shells in shallow cumulus using Doppler lidar and large-eddy simulation, Geophys. Res. Lett., 47, e2020GL089 699, https://doi.org/10.1029/2020GL089699, 2020.

Morton, B. R.: Buoyant plumes in a moist atmosphere, J. Fluid Mech., 2, 127–144, https://doi.org/10.1017/S0022112057000038, 1957.

Neggers, R. A. J., Siebesma, A. P., and Jonker, H. J. J.: A Multiparcel Model for Shallow Cumulus Convection, J. Atmos. Sci., 59, 1655–1668, https://doi.org/10.1175/1520-0469(2002)059<1655:AMMFSC>2.0.CO;2, 2002.

Nuijens, L. and Stevens, B.: The Influence of Wind Speed on Shallow Marine Cumulus Convection, J. Atmos. Sci., 69, 168–184, https://doi.org/10.1175/JAS-D-11-02.1, 2012.

Parker, M. D.: Relationship between System Slope and Updraft Intensity in Squall Lines, Mon. Wea. Rev., 138, 3572–3578, https://doi.org/10.1175/2010MWR3441.1, 2010.

Perry, K. D. and Hobbs, P. V.: Influences of Isolated Cumulus Clouds on the Humidity of Their Surroundings, J. Atmos. Sci., 53, 159–174, https://doi.org/10.1175/1520-0469(1996)053<0159:IOICCO>2.0.CO;2, 1996.

Peters, J. M.: The Impact of Effective Buoyancy and Dynamic Pressure Forcing on Vertical Velocities within Two-Dimensional Updrafts, J. Atmos. Sci., 73, 4531–4551, https://doi.org/10.1175/JAS-D-16-0016.1, 2016.

660 Peters, J. M., Hannah, W., and Morrison, H.: The Influence of Vertical Wind Shear on Moist Thermals, J. Atmos. Sci., 76, 1645–1659, https://doi.org/10.1175/JAS-D-18-0296.1, 2019a.

Peters, J. M., Nowotarski, C. J., and Morrison, H.: The Role of Vertical Wind Shear in Modulating Maximum Supercell Updraft Velocities, J. Atmos. Sci., 76, 3169–3189, https://doi.org/10.1175/JAS-D-19-0096.1, 2019b.

Rauber, R., Stevens, B., III, H. T. O., Knight, C., Albrecht, B. A., Blyth, A., Fairall, C., Jensen, J. B., Lasher-Trapp, S. G., Mayol-Bracero,
665 O. L., Vali, G., Anderson, J. R., Baker, B. A., Bandy, A. R., Burnet, F., Brenguier, J.-L., Brewer, W. A., Brown, P. R. A., Chuang, P., Cotton, W. R., Girolamo, L. D., Geerts, B., Gerber, H., Göke, S., Gomes, L., Heikes, B. G., Hudson, J. G., Kollias, P., Lawson, R. P., Krueger, S. K., Lenschow, D. H., Nuijens, L., O'Sullivan, D. W., Rilling, R. A., Rogers, D. C., Siebesma, A. P., Snodgrass, E., Stith, J. L., Thornton, D., Tucker, S., Twohy, C. H., and Zuidema, P.: Rain in shallow cumulus over the ocean - the RICO campaign, Bull. Amer. Meteor. Soc., 88, 1912–1928, https://doi.org/10.1175/BAMS-88-12-1912, 2007.

670 Rieck, M., Hohenegger, C., and van Heerwaarden, C. C.: The Influence of Land Surface Heterogeneities on Cloud Size Development, Mon. Wea. Rev., 142, 3830–3846, https://doi.org/10.1175/MWR-D-13-00354.1, 2014.

Romps, D. M.: A Direct Measure of Entrainment, J. Atmos. Sci., 67, 1908–1927, https://doi.org/10.1175/2010JAS3371.1, 2010.

Romps, D. M. and Charn, A. B.: Sticky Thermals: Evidence for a Dominant Balance between Buoyancy and Drag in Cloud Updrafts, J. Atmos. Sci., 72, 2890–2901, https://doi.org/10.1175/JAS-D-15-0042.1, 2015.

675 Rotunno, R. and Klemp, J. B.: The Influence of the Shear-Induced Pressure Gradient on Thunderstorm Motion, Mon. Wea. Rev., 110, 136–151, https://doi.org/10.1175/1520-0493(1982)110<0136:TIOTSI>2.0.CO;2, 1982.

Rousseau-Rizzi, R., Kirshbaum, D. J., and Yau, M. K.: Initiation of Deep Convection over an Idealized Mesoscale Convergence Line, J. Atmos. Sci., 74, 835–853, https://doi.org/10.1175/JAS-D-16-0221.1, 2017.

Sherwood, S. C., Hernandez-Deckers, D., Colin, M., and Robinson, F.: Slippery Thermals and the Cumulus Entrainment Paradox, J. Atmos.
680 Sci., 70, 2426–2442, https://doi.org/10.1175/JAS-D-12-0220.1, 2013.

Siebesma, A. P.: Shallow cumulus convection, in: Buoyant Convection in Geophysical Flows, edited by Plate, E., Fedorovich, E., Viegas, D., and Wyngaard, J., pp. 441–486, Springer Netherlands, 1998.

Siebesma, A. P. and Cuijpers, J. W. M.: Parametric Assumptions for Shallow Cumulus Convection, J. Atmos. Sci., 52, 650–666, https://doi.org/10.1175/1520-0469(1995)052<0650:EOPAFS>2.0.CO;2, 1995.

685 Siebesma, A. P., Bretherton, C. S., Brown, A., Chlond, A., Cuxart, J., Duynkerke, P. G., Jiang, H., Khairoutdinov, M., Lewellen, D., Moeng, C.-H., Sanchez, E., Stevens, B., and Stevens, D. E.: A Large Eddy Simulation Intercomparison Study of Shallow Cumulus Convection, J. Atmos. Sci., 60, 1201–1248, https://doi.org/10.1175/1520-0469(2003)60<1201:ALESIS>2.0.CO;2, 2003.

Smolarkiewicz, P. K. and Rotunno, R.: Low Froude number flow past three-dimensional obstacles. Part I: Baroclinically generated lee vortices, J. Atmos. Sci., 46, 1154–1164, https://doi.org/10.1175/1520-0469(1989)046<1154:LFNFPT>2.0.CO;2, 1989.

690 Stirling, A. J. and Stratton, R. A.: Entrainment process in the diurnal cycle of deep convection over land, Quart. J. Roy. Meteor. Soc., 138, 1135–1149, https://doi.org/10.1002/qj.1868, 2012.

Stull, R. B.: A fair-weather cumulus cloud classification scheme for mixed-layer studies, J. Climate Appl. Meteor., 24, 49–56, https://doi.org/10.1175/1520-0450(1985)024<0049:AFWCCC>2.0.CO;2, 1985.

Tang, S. L. and Kirshbaum, D. J.: On the sensitivity of deep-convection initiation to horizontal grid resolution, Quart. J. Roy. Meteor. Soc.,
695 146, 1085–1105, https://doi.org/10.1002/qj.3726, 2020.

Tian, Y. and Kuang, Z.: Dependence of entrainment in shallow cumulus convection on vertical velocity and distance to cloud edge, Geophys. Res. Lett., 43, 4056–4065, https://doi.org/10.1002/2016GL069005, 2016.

Wang, H. and McFarquhar, G. M.: Modeling aerosol effects on shallow cumulus convection under various meteorological conditions observed over the Indian Ocean and implications for development of mass-flux parameterizations for climate models, J. Geophys. Res., 113, D20 201, https://doi.org/10.1029/2008JD009914, 2008.

Wang, Y. and Geerts, B.: Humidity variations across the edge of trade wind cumuli: Observations and dynamical implications, Atmos. Res., 97, 144–156, https://doi.org/10.1016/j.atmosres.2010.03.017, 2010.

Weckwerth, T. M., Wilson, J. W., Wakimoto, R. M., and Crook, N. A.: Horizontal Convective Rolls: Determining the Environmental Conditions Supporting their Existence and Characteristics, Mon. Wea. Rev., 125, 505 – 526, https://doi.org/10.1175/1520-0493(1997)125<0505:HCRDTE>2.0.CO;2, 1997.

Wyant, M. C., Bretherton, C. S., and Blossey, P. N.: The Sensitivity of Numerical Simulations of Cloud-Topped Boundary Layers to Cross-Grid Flow, J. Adv. Model. Earth. Sy., 10, 466–480, https://doi.org/10.1002/2017MS001241, 2018.

Zhao, M. and Austin, P. H.: Life Cycle of Numerically Simulated Shallow Cumulus Clouds. Part II: Mixing Dynamics, J. Atmos. Sci., 62, 1291–1310, https://doi.org/10.1175/JAS3415.1, 2005.